Project Acronym:

BRAINSONIC (ENTERPRISES/0223/Sub-Call1/0057)

MRI-guided Focused Ultrasound robotic system for brain tumors.

Deliverable number: 5.2

Title: MRI evaluation of the thermal heating.

Prepared by:

Anastasia Antoniou (CUT)
Leonidas Georgiou (LINAC)
Antonis Christofi (LINAC)
Christakis Damianou (CUT)

Date: 28/09/2025

Funded by the European Union NextGenerationEU

Cyprus tomorrow RECOVERY AND RESILIENCE PLAN

Republic of Cyprus

RESEARCH & INNOVATION FOUNDATION

The BRAINSONIC project is funded by the Recovery and Resilience Facility of the NextGenerationEU instrument, through the Research and Innovation Foundation (RIF) of Cyprus.

Contents

1. EXECUTIVE SUMMARY

This deliverable presents the results of a comprehensive study on the thermal heating capabilities of the BRAINSONIC system in a high-field Magnetic Resonance Imaging (MRI) scanner, employing a variety of phantom models designed to simulate biological tissues. The study begins with a detailed description of the phantom models and experimental setups used for both manual and robotically assisted sonications, including the specifications of the ultrasonic transducers and the MRI sequences employed. Additionally, it outlines the techniques used to optimize MR thermometry.

Extensive experimentation was conducted to assess thermal effects and lesion formation in agar-silica phantoms using various Focused Ultrasound (FUS) protocols, with comparisons to outcomes in excised porcine tissue. Different combinations of acoustic power, exposure duration, and focal depth were tested to investigate their influence on lesion dynamics, while also evaluating the performance of the various ultrasonic transducers. In this context, the threshold thermal dose for effective lesion creation was identified, where "effective lesion creation" refers to lesions that are clearly identifiable on conventional MRI. The repeatability of thermal heating patterns was also evaluated.

Advanced imaging techniques were employed for both intra- and post-procedural assessments, with MR thermometry enabling precise temperature monitoring and high-resolution T2-weighted turbo spin echo (TSE) imaging used to track lesion development. The TSE imaging leveraged FUS-induced signal intensity variations to evaluate lesion dynamics, providing valuable insights into their temporal evolution and regression.

The evaluation then transitioned to more advanced models, including a head phantom with realistic geometry and tumor simulators. Various skull mimics, made from different materials and thicknesses, were integrated into the head phantom model and a series of sonications were performed to understand their impact on beam propagation and lesion creation at different focal depths, with unobstructed sonication serving as the reference for comparison. Additionally, a flow phantom was developed to simulate the dynamics of small-caliber vessel networks under FUS exposure. This model was specifically designed to account for heat dissipation effects and beam-vessel interactions, both of which could influence local heating. Lesion dynamics, targeting accuracy, and thermal diffusion were comprehensively investigated within these models.

While this deliverable primarily focused on the thermal effects of FUS, preliminary histotripsy experiments investigated the relationship between ultrasonic parameters and erosion patterns in less stiff agar phantoms, as well as the feasibility of MRI-based intraprocedural monitoring of histotripsy effects. In this context, histotripsy was evaluated as a potential application to enhance the capabilities of the BRAINSONIC system.

Dedicated sections follow for each of the above investigations.

2. MATERIALS AND METHODS

2.1 Phantom models used for thermal heating assessment

The employed phantoms and selection of recipes reported in this deliverable for testing various sonication protocols in the MRI setting were informed by the findings of deliverable 4.1 "Development of phantom with tumor mimics". As part of deliverable 4.1, seven (7) different phantoms were formulated using agar (Merck KGaA, Darmstadt, Germany) as the gelling agent. Pure agar gels were prepared at concentrations of 2, 4 and 6 % weight per volume (w/v). Phantoms containing a constant amount of 6 % w/v agar and increasing amount of silicon dioxide (Sigma-Aldrich, Missouri, USA) of 2, 4, 6, and 8 % w/v were also prepared. Their acoustic, thermal, and mechanical properties were characterized, and both the thermal behaviour and lesion visibility on post-sonication Turbo Spin Echo (TSE) images were evaluated. Relevant findings informed the development of both simple and more advanced phantoms with realistic geometry, which were utilized in this deliverable to comprehensively evaluate the thermal heating capabilities of the BRAINSONIC system. Specifically, a formulation containing 6% w/v agar and 4-6% w/v silica was identified as the most effective for mimicking soft tissue in FUS thermal applications. Based on this optimized composition, two types of phantom designs were created: a **simple rectangular model** and a **geometrically accurate model** incorporating a skull mimic (Head phantom), as illustrated in **Figure 1**.

Figure 1: *Photos of simple design and geometrically accurate (head) phantoms.*

Both phantom designs were developed in two versions: one with embedded tumor mimics and one without (plain phantom). For the tumor-embedded phantoms, spherical tumor mimics were composed of 6% w/v agar mixed with 4–6% w/v silica, while the surrounding matrix typically consisted of pure 6% w/v agar gel to facilitate tumor delineation on MRI images. The general aim was to achieve a higher silica concentration in the tumor region, given that silica was found to enhance ultrasonic absorption and improve visibility of FUS-induced lesions.

2.2 Experimental setup for phantom sonications in MRI

2.2.1 Employed ultrasonic transducers

Three single-element spherically focused ultrasound (FUS) transducers; constructed in-house using purchased piezoelectric elements, were employed in this study. Each transducer differed in design parameters such as operating frequency (F), aperture size/diameter (D), and radius of curvature (R). Details of their specifications, including manufacturer and calculated f-number, are summarized in **Table 1** below. All transducers achieved an acoustic efficiency of approximately 30% and were powered by an external RF amplifier (AG1016, AG Series Amplifier, T&C Power Conversion, Rochester, NY, USA) using MR-compatible shielded cables, ensuring safe operation within the MRI environment.

***Table 1**: Specifications of Ultrasonic Transducers Used for Thermal Investigations.*[1]

Trans. No.	F (MHz)	D (mm)	R (mm)	f-number	n (%)	Manufacturer
1 (id57)	2.75	50	65	1.3	30	Piezo Hannas, Wuhan, CN
2 (id60)	1.1	90	100	1.1	30	Zibo Yuhai, Shandong, CN
3 (id49)	1.0	50	80	1.6	32	Piezo Hannas, Wuhan, CN
4 (id61)	2.5	100	100	1.0	30	Zibo Yuhai, Shandong, CN

For each transducer, the focal intensity was calculated by dividing the applied acoustic power by the effective area at the focal point, which is given by $A = \pi r^2$, where r is defined as $\frac{\lambda R}{2D}$.

2.2.2 Manual setup for phantom sonications in MRI

The agar phantom and ultrasonic transducer were secured in custom-designed holders, which were mounted on an acrylic water tank, as illustrated in the Computer-Aided Design (CAD) diagram shown in **Figure 2**. This configuration allowed for effective ultrasound transmission in a water bath. All structural components of the assembly were 3D printed using MRI-compatible Polylactic Acid (PLA) material on a professional Fused Deposition Modeling (FDM) printer (Raise3D E2, Raise3D, CA, USA). The phantom holder allows for manual movement along the Z-axis, providing a single degree of freedom. Meanwhile, the transducer holder is engineered to position the transducer below the phantom, with manual adjustments available along two perpendicular axes: vertical (Y-axis) for focal distance (FD) control, and horizontal (X-axis) for lateral positioning. The coordinated movements of both holders enable precise placement of the focal point within the phantom. In this context, Focal Depth (FD) refers to the depth within the phantom where the focus is located, specifically the distance between the bottom of the phantom and the focal center. To assist in accurate positioning during manual adjustments, markers were placed at 1 mm intervals. The setup was designed to be lightweight and portable, allowing for easy transfer into an MRI environment.

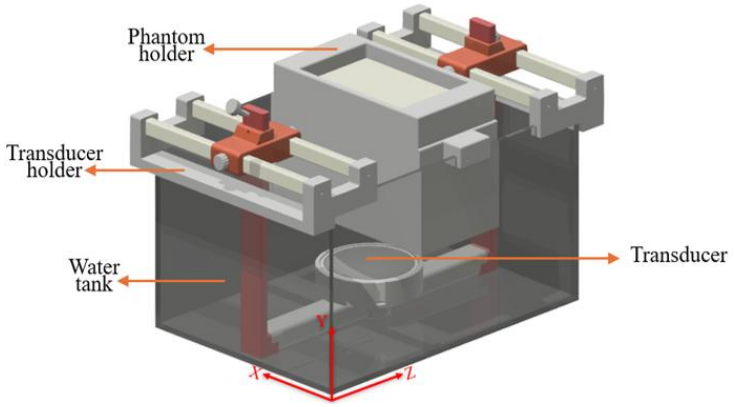

***Figure 2**: CAD drawing of the setup for phantom sonications.*

All evaluations were conducted in the 3T MRI scanner (Magnetom Vida, Siemens Healthineers, Erlangen, Germany). The water tank with integrated compartments, as detailed earlier, was placed on the MRI table, with a body coil (Body_18, Ultraflex small/large 18-channel coil, Siemens Healthineers) positioned above the setup, ensuring there was no direct contact between the coil and the phantom. The arrangement of the setup within the MRI environment is depicted in **Figure 3A**. The transducer was connected to the AG1016 RF

[1] F: Frequency, D: Diameter, R: Radius of Curvature, n: Efficiency

amplifier (T & C Power Conversion, Inc., Rochester, USA) located outside the MRI room via specially shielded cables. An indicative axial T2-Weighted (T2-W) TSE image showing the placement of a plain agar-based phantom above the transducer and through-water coupling is shown in **Figure 3B**. Notably, such images served as references for checking/ adjusting the focal point location and ensuring proper coupling (i.e., absence of bubbles), and were also used for comparison with post-sonication images.

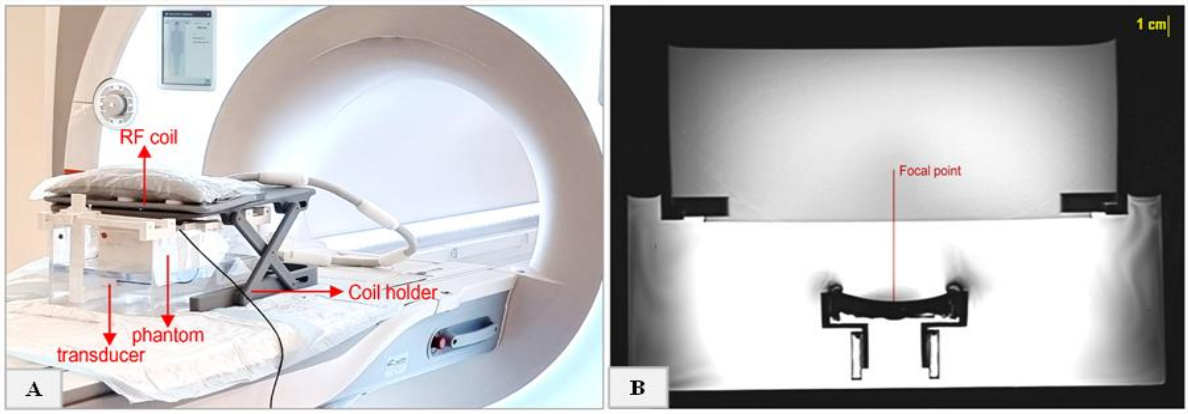

***Figure 3**: A) Manual setup for phantom sonications arranged in the MRI setting. B) T2-W TSE imaging of the setup showing phantom and transducer arrangement in the water tank.*

2.2.3 Setup for robotically assisted phantom sonications in MRI

The experimental setup, shown in **Figure 4**, included the developed 4-degree-of-freedom FUS robotic device seated on the MRI couch, featuring an acoustic opening located directly above the transducer's operating area. The phantom was securely positioned over this acoustic opening, and degassed water in the tank ensured optimal ultrasonic coupling with the transducer. The UltraFlex imaging coil (Siemens Healthineers) was placed a short distance above the phantom, supported by a dedicated plastic structure, to enable precise imaging without potential vibrations from the phantom affecting it. This setup also minimized interference from the mechatronic components by keeping them outside the imaging coil, ensuring clear imaging results.[1]

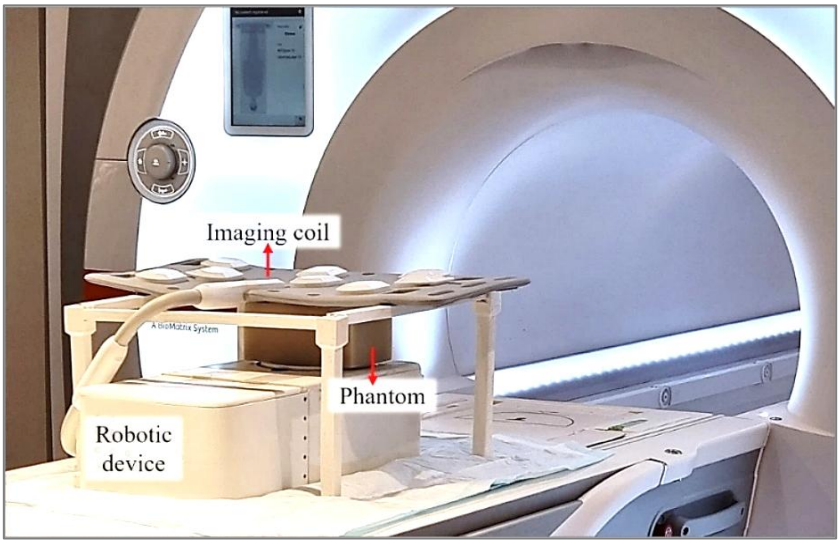

***Figure 4:** Experimental setup for robotically assisted phantom sonication arranged on the MRI table, with the agar-based phantom placed over the acoustic opening of the employed robotic device.*

2.2.4 Employed sequences for intra- and post-procedural MRI assessment

Thermal mapping was performed dynamically using the accompanying treatment planning-monitoring software. A series of Fast Low Angle Shot (FLASH) images were acquired with a temporal resolution of 2.4 s during and shortly after sonication, utilizing the parameters listed in **Table 2**.

***Table 2**: FLASH sequence parameters for MR thermometry.*[2]

TR (ms)	TE (ms)	NEX	FA (°)	Acq. time (s)
25 ms	10 ms	1	30	2.4
FOV (mm^2)	ETL	pBW (Hz/Pixel)	ST (mm)	Matrix
280 x 280	1	250	3-8	96 x 96

The proton resonance frequency (PRF) shift method was used to determine the developed temperatures within the region of interest.[2] This technique leverages the principle that the PRF shifts with changes in temperature. By comparing the phase of images acquired at an initial baseline temperature (φ_0) to those obtained at various times throughout the sonication (φ), the phase differences ($\varphi - \varphi_0$) were converted into temperature changes (ΔT) using a previously established equation.[2] Specifically, the following equation (1) applies:

$$\Delta T = \frac{\varphi - \varphi_0}{\alpha \, \gamma \, B_0 \, TE} \quad (1)$$

In this equation, α is the PRF shift coefficient, γ denotes the gyromagnetic ratio, and B_0 is the local magnetic field strength. Based on the acquired data, the software also calculated the accumulated thermal dose using the method outlined by Sapareto and Dewey,[3] with a PRF constant of −0.0094 ppm/°C, a value representative of human tissues. According to this method, the cumulative equivalent minutes at 43°C (CEM43°C) is given by:

$$\mathrm{CEM43°C} = \sum_{t=0}^{t=final} R^{43-T} \Delta T \quad (2)$$

where the variable T denotes the average temperature during the time interval and R the temperature-dependent factor affecting the rate of cell death. This parameter takes the value 0.25 at temperatures under 43°C and 0.5 when the temperature surpasses 43°C. The standard thermal dose threshold for achieving coagulative tissue ablation was defined as 240 CEM43°C,[4] and this value was used to generate thermal necrosis maps. Importantly, in high-intensity FUS treatments, a temperature of 55°C sustained for at least 1 second is considered sufficient to induce immediate cell death and coagulative necrosis.[5] The resulting thermal data were visualized as color-coded maps, illustrating estimated temperatures and logarithmically scaled thermal doses. Color gradients ranged from blue (indicating lower values) to red (indicating higher values). The threshold for cellular thermal damage (240 CEM43°C) was also indicated on the corresponding plots.

Upon completion of each sonication protocol, the phantom was immediately imaged using a high-resolution T2-W TSE sequence to assess lesion formation and extent, utilizing the parameters listed in **Table 3**. It is important to clarify that the term ‘lesion’ refers to a contrast

[2] TR: Repetition time, TE: Echo time, NEX: Number of averages, FA: Flip angle, FOV: Field of View, ETL: Echo train length, pBW: Pixel Bandwidth, SL: Slice thickness.

change (signal enhancement) caused by FUS energy deposition, which gradually fades over time, independent of the creation of ablative temperatures.

***Table 3**: Parameters of T2-W TSE sequence.*

TR (ms)	TE (ms)	NEX	FA (°)	Pixel spacing (mm)
3000	52	1/2	110	0.5
FOV (mm^2)	ETL	Matrix	ST (mm)	pBW (Hz/Pixel)
260 x 260	30	256 x 256	3	250

2.3 MR Thermometry Optimization

2.3.1 Thermometry sequence optimization

Prior to the main experiments, an evaluation to optimize MR thermometry was performed by adjusting key imaging parameters (TR, TE, ST, matrix size, and FA) of the reference FLASH sequence outlined in **Table 2** (with ST of 2 mm). A simple rectangular phantom model, composed of 6% w/v agar and 4% w/v silica, along with transducer No. 1 (2.7 MHz), were employed in the setup depicted in **Figure 3**. Imaging was conducted using the UltraFlex Small 18-channel coil (Siemens Healthineers). Parameters were changed as follows: TR = 20 and 15 ms, TE = 5, 15, and 20 ms, ST = 6, 9, and 12 mm, matrix size = 64×64 and 128×128, and FA = 20°, 30°, 35°, and 40°. Each parameter was varied while keeping the others constant to assess its individual impact on the signal to noise ratio (SNR) and overall image quality. The goal was to determine which combination of these factors results in the highest SNR, thereby improving the accuracy and reliability of temperature measurements.

2.3.2 Calculation of PRF Coefficient for Agar-Silica Phantom

This experimental part aimed to determine the PRF shift coefficient (α) for the agar-based phantom containing 6 % w/v agar and 4 % w/v silica, which was identified as suitable for sufficiently mimicking soft tissue properties. The phantom was sonicated at a typical electric power of 100 W (ac. power of 30 W) using transducer No.1 (Table 1) operating at 2.75 MHz (n=5). The focal point was set at 65 mm. Initially, a benchtop experiment was conducted, where focal temperatures changes were recorded using a thermocouple (5SRTC-TT-K-30-36, type K insulated beaded wire, Omega Engineering, Norwalk, USA). According to the PRF method, temperature changes (ΔT) within a region of interest induce a shift in the proton PRF in that region, which is observed as a phase difference ($\Delta\varphi$) in MR images acquired during sonication. Accordingly, the thermocouple measurements were correlated with the corresponding phase differences derived from FLASH-based PRF thermometry using the 3T Siemens MRI scanner, in accordance with Equation (1). Rearranging this equation yields the PRF shift coefficient (α), as shown in Equation (3):

$$a = \frac{\varphi(T) - \varphi(T_0)}{\Delta T \, \gamma \, B_0 \, TE} \tag{3}$$

The parameters of employed sequence are listed in **Table 2**, with the ST set to 8 mm. The relevant experimental setup can be seen in **Figure 3**.

2.4 Thermal Effects of FUS in Agar-Silica Phantoms

2.4.1 Threshold for effective lesion creation

The threshold for lesion creation in the 6% w/v agar and 4% w/v silica phantom was investigated using transducer No. 3, operating at 1 MHz (**Table 1**). This transducer was chosen for its broader focus, which results in the creation of larger lesions that are easier to detect, ensuring reliable threshold determination in MRI. The applied acoustic power was gradually increased from 26 to 46 W, while maintaining a constant exposure time of 20 s. Based on the focal area (A) of approximately 4.3 mm², the resulting focal intensities ranged from 600 to 1050 W/cm². For each level of applied power, the peak focal temperature (starting from a baseline of 19°C) and the thermal dose accumulated in the phantom were calculated to identify the threshold at which a lesion becomes visible on T2-W TSE images using the optimized sequence (**Table 3**). The authors established that for precise measurement of lesion size, the lesion must cover at least 4 pixels in diameter, which was used to define the threshold for effective lesion formation.

2.4.2 Repeatability of Phantom's Thermal Response

Transducer No.1 (Table 1) operating at 2.75 MHz was selected to evaluate the repeatability of heating in the selected phantom (6% agar, 4% silica) because of its well-defined focus, which ensured accurate and localized heating. An acoustical power of 45 W, corresponding to a focal intensity of ~9790 W/cm^2, was delivered for 60 s, at a FD of 3 cm (n=5). Notably, the duration of 60 s was selected to provide enough thermal energy to the target, in accordance with the thermal ablation objectives. The temperature profiles recorded with MR thermometry during the five sonications were compared to evaluate repeatability.

2.4.3 Thermal Mapping and Lesion Detection by MRI

A series of sonication experiments were conducted in the 3T scanner using the simple design agar-silica phantom. Thermal effects during sonication were recorded with FLASH based thermometry, while high-resolution imaging was performed afterward to visualize lesions using conventional T2-W TSE imaging. This sequence was also occasionally used intra-procedurally to monitor lesions based on signal intensity changes. The selected ultrasonic parameters fell within the typical range for high-intensity FUS applications, with acoustic intensities ranging from 500 to 20,000 W/cm² and durations from 1 to 60 s.[6]

2.4.3.1 Effect of sonication parameters on lesion dynamics

Electric power levels ranging from 50 to 400 and exposure times between 5 and 70 s were tested with the different transducers to evaluate the influence on thermal effects and the resulting lesion characteristics on T2-W TSE images. Each parameter (power and time) was varied independently, while the focal depth remained constant. It is noted that the maximum power for each transducer was set according to its tolerance threshold. Additionally, sonications were performed at various focal depths (based on the radius of curvature for each transducer) to assess the transducer's focusing performance at different depths and to evaluate the impact of attenuation on lesion formation. Lesion dynamics (shape and size) were assessed in response to varying ultrasonic parameters. Lesions were considered measurable if their length or diameter was at least 2 mm (equivalent to 4 pixels, with a pixel size of 0.5 mm). The

pixel intensity threshold for measuring lesion size was determined for each image acquisition, using a contrast-to-noise ratio (CNR) greater than 80 to ensure reliable lesion detection through visual inspection. The diameter of the lesion was measured at its midpoint. Following single spot sonications, grid sonications were executed using the BRAINSONIC robotic system and software.

2.4.3.2 Regression of lesions over time

The regression of lesions induced by high-power FUS in the phantom was monitored over time using T1-W and T2-W TSE sequences. A series of post-sonication images were taken at 2-minute intervals to observe the reduction in lesion size and the time required for complete disappearance, while also evaluating the phantom's reusability. In this context, reusability refers to the phantom's capacity to recover to its initial condition after being subjected to FUS-induced damage, allowing it to be reused and re-sonicated multiple times. Furthermore, CNR measurements were performed to provide quantitative data. The specific parameters of the T2-W sequence are listed in Table 3. Note that the pixel size of 0.5 mm, corresponds to a matrix size of 512x512 after post-processing. The image acquisition time was approximately 1.5 min. The relevant parameters for the T1-W TSE sequence were TR=1500 ms, TE=7.8 ms, FA=150°, NEX=1, and ETL= 3, with a similar FOV, matrix size, and slice thickness. CNR was calculated using the following Equation (4), where SI_{lesion} is the mean signal intensity from a region of interest placed in the lesion, $SI_{phantom}$ represents the signal intensity in the surrounding area, and σ_{noise} is the standard deviation of the background noise.

$$CNR = \frac{(SI_{lesion} - SI_{phantom})}{\sigma_{noise}} \quad (4)$$

2.5 Phantom Vs Excised Porcine Tissue: Thermal Response and Lesion Formation

During this experimental phase, identical ablation protocols were tested on the phantom containing 6% w/v agar and 4% w/v silica and excised porcine tissue. The purpose was to compare the effectiveness of lesion formation in grid patterns between the two models, assessing both the consistency of lesion formation and its accuracy relative to the target FD, while also identifying any potential shifts. For grid sonications, durations of up to 30 s were preferred, with 60 s of cooling between sonications to reduce heat dissipation and prevent excessive heat accumulation in off-target areas.

2.6 Near field heating

This experiment aimed to assess near-field heating phenomena in the phantom (6% w/v agar, 6% w/v silica) by monitoring lesion formation in grid patterns within the 3T MRI scanner. Sonications were performed using Transducer No.2 (1.1 MHz), integrated into the BRAINSONIC robotic system driven by dedicated electronic driving system (Serial number: DS003). Ultrasonic energy was delivered in grid patterns with varying sonication settings to study their effect on lesion overlap, distinctness, and size. Specifically, grid sonications were performed using a 1×8 grid with a 4 mm step size and a focal depth of 50 mm, applying varying sonication parameters to assess the impact of exposure time and delay intervals. The electric/acoustic power was set to 300/90 W, with sonication times of 10 s, 20 s, and 30 s.

Delay intervals between sonications were varied at 20 s, 60 s, 120 s, and 200 s. The different protocols combined these parameters to evaluate their effects on lesion formation and thermal response. High-resolution MR imaging was performed throughout the grid operation (during the commanded time delay) to assess lesion formation. The relevant experimental setup is illustrated in **Figure 4**.

2.7 Tumor phantom model: MRI assessment of Thermal effects and Lesion formation

This experimental section aimed to assess the thermal effects induced by high-power FUS sonications within a tumor phantom model. This model included a 2-cm diameter tumor mimic; composed of 6% w/v agar and 6% w/v silica, which was embedded at a depth of 4.5 cm within the bulk phantom material (6% w/v agar). MRI-guided sonications were conducted with Transducer No. 4, targeting the tumor mimic, in accordance with the procedure used for the plain phantom. Electrical power levels ranging from 250 to 400 W (corresponding to 75–120 W acoustic power) were applied for 60 s at a fixed FD of 45 mm to explore variations in the resulting focal temperatures (via PRF thermometry) and lesion dynamics (via high resolution T2-W TSE imaging). For reference, sonication at the maximum power of 400 W was also conducted within the background (non-tumor) material.

2.8 Flow phantom

2.8.1 Development Requirements

The steady flow phantom system was designed with specific requirements to ensure optimal performance for its intended use: [a] Materials and design that ensure MRI compatibility, including sufficiently long tubing (8 m), as well as compact, and lightweight structure. [b] Time- and cost-efficient fabrication for practicality and economic feasibility. [c] Sufficient structural integrity to withstand repeated use and maintain performance during prolonged experiments. [d] A wall-less design to prevent attenuation caused by the tubing. [e] Development of a multi-channel network (<1 mm diameter) to mimic flow dynamics in small-caliper vessel networks.

2.8.2 Flow phantom Design

The tissue-mimicking material for the flow phantom was prepared using the typical concentrations of 6% w/v agar and 4% w/v silicon dioxide (dissolved in degassed water), as this composition has been shown to closely approximate essential application-relevant properties of real tissue, particularly acoustic, thermal, and MR relaxation properties.[7] Channels were formed by securing flexible cables (0.8 mm thickness) along winding, non-linear paths within a dedicated container. The agar-silica solution was then added and allowed to solidify, forming a phantom measuring 6 cm in width, 8 cm in length, and 8 cm in height. Once the solution had fully solidified, the cables were removed, leaving curved channels within the material. Another phantom with identical dimensions and composition was created, but without channels. This version served as a static (no vessel) phantom for comparison purposes.

2.8.3 Flow System Setup

The phantom container was designed with protrusions to securely attach the inlet and outlet tubes (4-mm diameter), which were connected to a peristaltic pump (Masterflex L/S, Model 7518-60, Cole-Parmer, Illinois, USA), allowing for water circulation through the channels. Notably, the inlet and outlet tubes each had a length of 8 m to allow for proper setup in the MRI setting. The phantom container also featured two protruding extensions that can be movably attached to the periphery of a water tank, enabling the phantom to be positioned and adjusted along the MRI's Z-axis (front to back). Additionally, a custom-made plastic structure was attached to the tank to secure the transducer beneath the phantom. This setup allowed for left-right movement of the transducer, as well as vertical adjustment (up and down) to modify the focal depth within the phantom. The final flow phantom system can be seen in **Figure 5**a.

2.8.4 Evaluation of Imaging Features and Thermal response

High resolution images of the phantom were acquired with a T2-W TSE sequence in the 3 T Magnetom Vida scanner (Siemens Healthineers) with the following parameters: TR of 3100 ms, TE of 62 ms, FA of 110°, NEX of 3, pBW of 256 Hz/pixel, ST of 1.5 mm, matrix of 256 × 256, and ETL of 14, using the UltraFlex large coil for signal reception. Computed Tomography (CT) scans of the phantom were also acquired in a Siemens CT scanner (SOMATOM Force), with a slice thickness of 0.6 mm, a tube voltage of 120 kVp, and a current of 96 mA.

The phantom was exposed to 15-45 W acoustic power, which translates to focal intensities in the range of 3250 to 9800 W/cm^2, using transducer No.1 (2.75 MHz). The exposure lasted 30 s at higher power levels and up to 60 s at the lowest tested acoustic power. The focal point was set at 4 cm, centrally within the simulated vessel network. Continuous flow, with a steady rate of 38 mL/min (corresponding to 9.6 mL/min per 100g of phantom material) was maintained throughout the experiment. This flow rate reflects conditions in regions that primarily depend on small-caliber vessels, where blood flow is generally lower than in highly metabolic organs.[8,9] Heating-induced phase shifts ($\Delta\varphi$) measured via FLASH-based MR thermometry were correlated with temperature changes (ΔT) using equation (1). **Figure 5b** shows a photo of the flow phantom experiment conducted in the 3T MRI scanner. The water tank was positioned on the MRI couch, with the inlet and outlet tubes extending through a penetration panel in the wall to connect the phantom to the peristaltic pump located outside the MRI room.

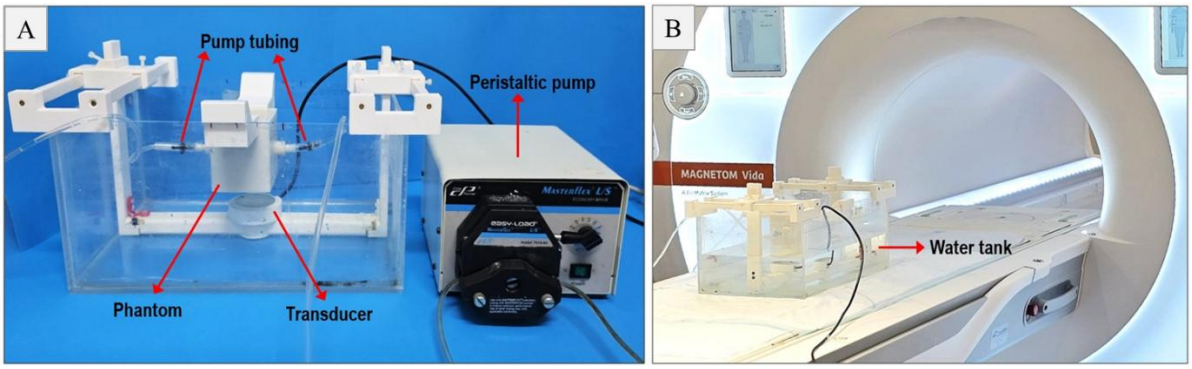

***Figure 5**: Photos of the experimental setup arranged in A) laboratory and B) MRI settings.*

2.9 Head phantom model with tumor simulators

2.9.1 Phantom Characteristics and Experimental Integration

Experiments initially conducted in the simple phantom model were subsequently extended to the head phantom. As described in deliverable 4.1, this phantom features a precise skull replica, generated by extracting anatomical models from CT scans of a healthy volunteer. These were postprocessed to isolate the bone and 3D printed using Acrylonitrile Butadiene Styrene (ABS) thermoplastic (F270 FDM printer, Stratasys, Minnesota, USA). A circular section was removed from the skull model (referred to as the skull insert) to create an aperture of approximately 28 cm². This modification allowed tumor sonication with or without skull interference, enabling the use of skull mimics made from various 3D-printable polymers to assess their impact on energy deposition to the target.

The skull model was filled with a brain tissue-mimicking material containing a tumor mimic, both made from agar gels. The method involved solidifying an aqueous solution of 6% weight per volume (w/v) agar (Merck KGaA, Darmstadt, Germany) and 4% w/v silica (Sigma-Aldrich, Missouri, USA) in a releasable mold to create a spherical tumor model, which was then embedded in the normal tissue phantom while in a liquid state. A solution of 6% w/v agar was used to form the healthy tissue compartment.

For each sonication protocol tested, the tumor mimic was embedded at a specific distance from the circular opening on the skull model. Therefore, different phantoms were developed to position the tumor center at depths ranging from 3.5 to 7 cm, facilitating a comprehensive assessment of targeting efficacy across both shallow and deep phantom layers. In each case, a tumor diameter of either 2 or 3 cm was selected. The relevant experimental setup aligns with arrangement shown in **Figure 3** and **Figure 4** for manual and robotic assisted sonications respectively, though the head phantom was used instead. Photographs of the setup with the head phantom are shown **Figure 6** and **Figure 7**. Note that the phantom is positioned to simulate a laterally lying patient for practical reasons, with the aperture (at the temporal-parietal region) facing the transducer.

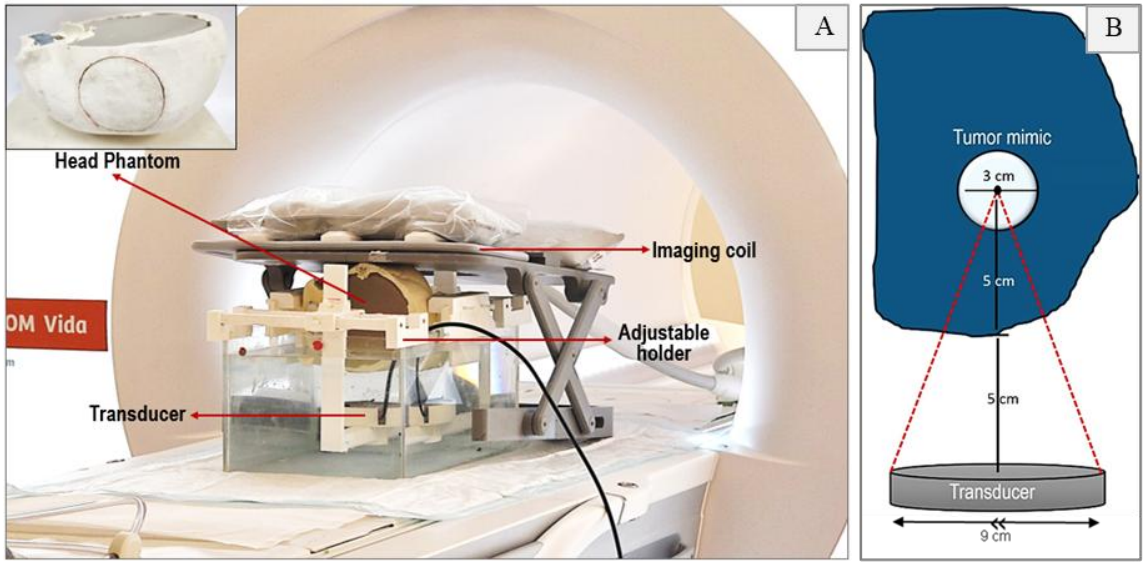

***Figure 6**: A) Photo of the water-filled tank housing the phantom-transducer setup, positioned on the patient couch for MRI-monitored sonications, including a close-up photo of the head phantom model. B) Diagram illustrating the concept of Transducer No. 2 targeting a 3-cm tumor mimic at the center.*

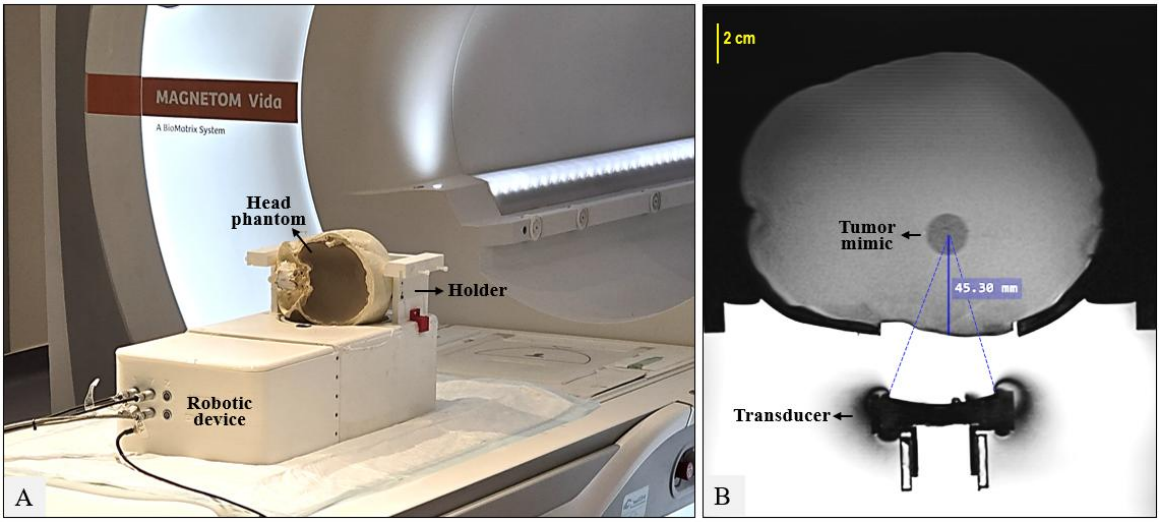

***Figure** 7: (A) Photo of the basic setup components arranged in the MRI setting for robotic-assisted sonications in the head phantom. (B) T2-W TSE axial image of the head phantom, with the transducer's focal spot adjusted at the tumor center.*

2.9.2 Single and grid sonications: Effect of sonication parameters

Single sonications were initially performed targeting the tumor mimic, with variations in power and duration to assess their impact on lesion dimensions and targeting accuracy. Subsequently, grid sonications were conducted to evaluate the feasibility of covering the entire tumor mimic through transducer motion, utilizing the robotic device. Planning for these sonications was performed using the accompanying MRI-guided Focused Ultrasound (MRgFUS) software, based on preoperative MR images of the experimental setup.

The applied focal intensities ranged from approximately 1,800 to 6,400 W/cm², with exposure times varying from 20 to 60 s. FDs of 3.5 to 7 cm were tested, each using the appropriate phantom with the tumor mimic embedded at the corresponding depth, as explained previously. Depending on the FD, either transducer No. 3 (80-mm radius of curvature) or the larger transducer No. 2 (100-mm radius of curvature), both operating at 1 MHz, was employed. Identical sonications were conducted in an unobstructed field (i.e., without skull interference) and individually across the three 1-mm thick skull mimics, each fixed at the corresponding aperture.

2.9.3 Beam Obstruction by Skull Mimic

2.9.3.1 Effect of different printing materials

Sonications were conducted with Transducer No.3 (1 MHz) in free field, as well as through 3D-printed skull mimics made from different thermoplastic materials, with MR thermometry employed for precise temperature measurements. The thermometry results were compared between the skull mimics and the free field conditions (i.e., no skull mimic). Specifically, the following printing materials were selected: Resin (Photon M3 Max SLA printer, Anycubic, China), ASA (F270 FDM industrial 3D printer, Stratasys, Minnesota, USA), and TPU (3 Extended Ultimaker FDM printer), all printed in the described circular shape with a thickness of 1 mm. A photo of the various 3D printed skull inserts is shown in **Figure 8**.

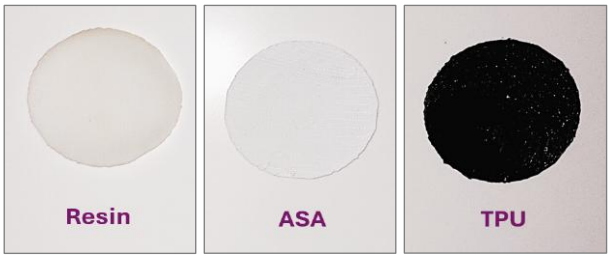

***Figure 8**: Photo of the 3D printed thermoplastic circle-shaped skull mimics.*

2.9.3.2 Effect of Skull Thickness

The resin-based skull mimic demonstrated the best performance among the tested plastics and was therefore selected for further experimentation. Dedicated experiments were subsequently conducted using this material, including tests with varying thicknesses. All the sonications were executed with a single-element concave transducer No.2 (1.1 MHz). Acoustic power levels of 60 and 120 W, corresponding to focal (spatial peak) intensities of approximately 3200 W/cm² and 6400 W/cm², were tested, with a sonication time of 60 s for both conditions. The focal depth was set at 5 cm by adjusting the distance between the transducer and the bottom surface of the phantom. Each protocol was initially tested without skull interference (through the designated aperture on the skull model). It was then tested with resin skull inserts of increasing uniform thickness (1, 2, and 3 mm) obstructing the beam, followed by testing with a realistic skull insert (featuring varying thickness across its surface). A total of 10 measurements were conducted for each condition. ANOVA followed by post-hoc (Tukey's Honest Significant Difference; HSD) analysis was performed to assess the significance of recorded temperature changes among the different groups.

2.10 Sonication in Lamb brain

The thermal protocols were tested in real lamb brain tissue for comparison purposes. Sonications were delivered through an acoustic window created on the skull. Thermal effects by high-power sonications at an electric/acoustic power of 100/35 W for 60 s, with the FD adjusted at 20 mm using transducer No. 3 (1 MHz) was monitored in the 3T MRI scanner. **Figure 9** shows a T2-W TSE sagittal image of the experimental setup, illustrating the location of the transducer relative to the lamb's head, as well as a coronal view of the head.

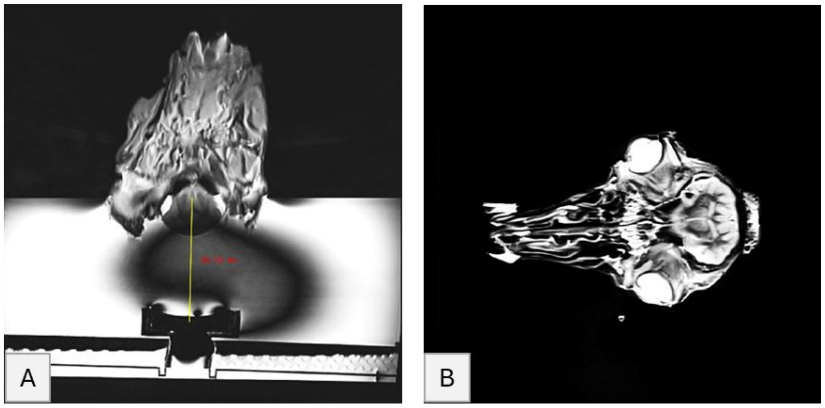

***Figure 9**: A) Sagittal T2-W TSE image of the experimental setup, showing the transducer's position relative to the target in lamb brain tissue. B) Coronal T2-W TSE image depicting the lamb's head.*

2.11 Preliminary Testing of Histotripsy Protocols

2.11.1 Histotripsy phantom preparation

A pure agar gel, proven to be susceptible to cavitation-induced damage, served as the target for all sonications. The gel was prepared with a 2% agar concentration (Merck KGgA, Darmstadt, Germany), dissolved in water, according to the procedure outlined in previous literature.[10] The decision to use this specific phantom formulation was informed by prior findings indicating that lower agar concentrations (e.g., 2% w/v) are more susceptible to cavitation-induced damage, whereas stiffer phantoms (≥2.5% w/v) exhibit greater resistance to erosion.

The fabrication process was straightforward, involving a heating and a cooling cycle, with continuous automated stirring to ensure a homogeneous environment for histotripsy experiments. The agar gel was molded in a dedicated plastic container with dimensions of 10 cm (width) × 20 cm (length) × 10 cm (height), featuring handles for attachment to the rest of the setup and allowing for the removal of its bottom surface for bottom-up sonications. The density of pure 2% agar gel was measured at 901 ± 3 kg/m³ (n=10), while its Young's modulus has been reported to be around 40 kPa.[11]

2.11.2 Laboratory evaluation Effect of ultrasonic parameters on phantom erosion

Histotripsy sonications were performed in the 2% agar phantom using transducer No.1 (2.6 MHz) in a laboratory setting, with lesion formation assessed post-exposures through imaging and gross morphology. The relevant experimental setup can be seen in **Figure 10**. Before the experiments, the phantom was submerged in water and degassed for 3 hours in a vacuum chamber (VC2523AG, Vacuum Chambers, Jodlowa, Poland) with a dual-stage vacuum pump (VP260, Vacuum Chambers) at a pressure of -1 bar.

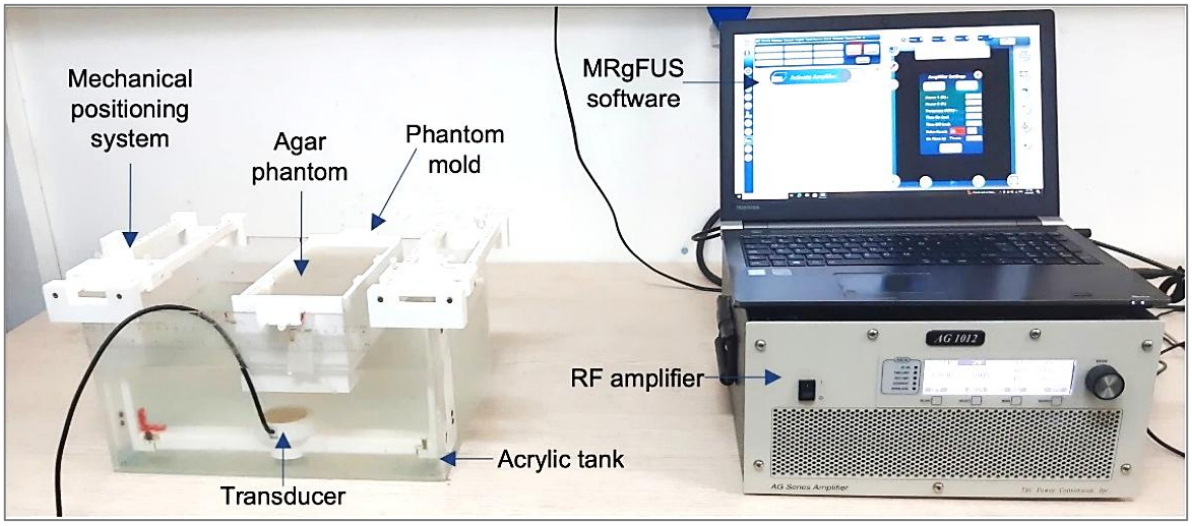

***Figure 10**: Experimental setup used for histotripsy sonications on agar-based phantoms.*

Ultrasonic protocols were applied at different single-spot treatment locations by appropriately aligning the transducer at varied sites below the bottom surface of the agar-based phantom. This was achieved by laterally moving the transducer using the mechanical positioning system and sliding the mold couplings along the tank's edge, thus moving the longitudinal axis of the phantom sideways. For all tested protocols, the transducer focus was set 2 cm deep within the phantom.

The effect of acoustic power, pulse repetition period (PRP), and pulse count, i.e., number of pulses (N) on phantom erosion and lesion dimensions was investigated by varying these parameters as shown in **Table 4**.

***Table 4**: Effect of sonication parameters on phantom erosion and lesion dimensions.*[3]

DF (%)	PD (ms)	PRP (ms)	N	Power (W)
2	10	500	1000	200, 210, 215
	15	750	1500	
2	5	250	200, 500, 1000	215
	10	500		
	15	750		

After completion of the sonications, the phantom was removed from the acrylic tank and positioned on the table of the Siemens MRI scanner to assess histotripsy-induced damage. Imaging was performed using a 64-channel head-and-neck coil (Siemens Healthineers) and a high-resolution T2-W TSE sequence with the following scan parameters: TR = 2120 ms, TE = 82 ms, FA = 149º, NEX = 2, pBW = 219 Hz/Pixel, FOV = 220×220 mm^2, ST = 3 mm, Acquisition Matrix = 416×416, and ETL = 13.

2.11.3 MRI monitoring of Histotripsy lesion formation in phantom

The setup for phantom sonications in the MRI scanner (3T, Magnetom Vida, Siemens Healthineers, Erlangen, Germany) employed a standard water tank arrangement, as shown in **Figure 3**. Pulsed FUS was applied using transducer No. 1 (2.75 MHz), with a DF of 2% and a PRP of 1 s, based on laboratory experimental results. The employed amplifier (AG1016, AG Series Amplifier) was set to deliver 450 W, corresponding to an effective acoustic power of 135 W. This translated to a spatial peak pulse average intensity (SPPA) of 29.4 kW/cm^2 and a spatial peak temporal average intensity (SPTA) of 587 W/cm^2. A total of 1000 to 2000 pulses were delivered at a focal depth (FD) of 2.5 cm.

Histotripsy-induced structural changes in the phantom were tracked during sonication through the acquisition of axial T2-W TSE images at 10-s intervals with: TR = 2,000 ms, TE = 52 ms, NEX = 1, FA = 110°, Matrix size = 192 x 192, ST = 4 mm, ETL = 30, pBW = 250 Hz/pixel, and FOV = 260 x 260 mm^2. The selected sequence parameters represent a balance between image quality, considering both resolution and signal-to-noise ratio (SNR), and acquisition time. The chosen acquisition time of 10 s per image, corresponding to ten FUS pulses, was considered sufficiently short given the inherently slow nature of the process, where this duration is generally insufficient to produce observable outcomes. PRF shift thermometry enabled monitoring the developed temperatures with a temporal resolution of 2.4 s, utilizing the optimized FLASH sequence (**Table 2**) with a ST of 6 mm. Thermal maps were generated during sonication and for approximately 250 s afterward. Coronal and axial T2-W TSE scans were repeated post-sonication using a modified sequence to enhance SNR and resolution. This was achieved by increasing the TR to 2,600 ms and NEX to 2, as well as using a larger matrix size of 256 × 256, while keeping all other parameters unchanged.

[3] DF: Duty Factor, PD: Pulse Duration, PRP: Pulse repetition period, N: pulse count.

3. RESULTS

3.1 Thermometry Optimization

3.1.1 Thermometry sequence optimization

The results of the MR thermometry optimization experiment are shown in **Figure 11**, which illustrates the SNR values obtained for the various tested FLASH sequence parameters. The bar chart highlights the impact of varying TR, TE, ST, matrix size, and Flip angle on phantom SNR, demonstrating that slice thickness was the most critical factor.

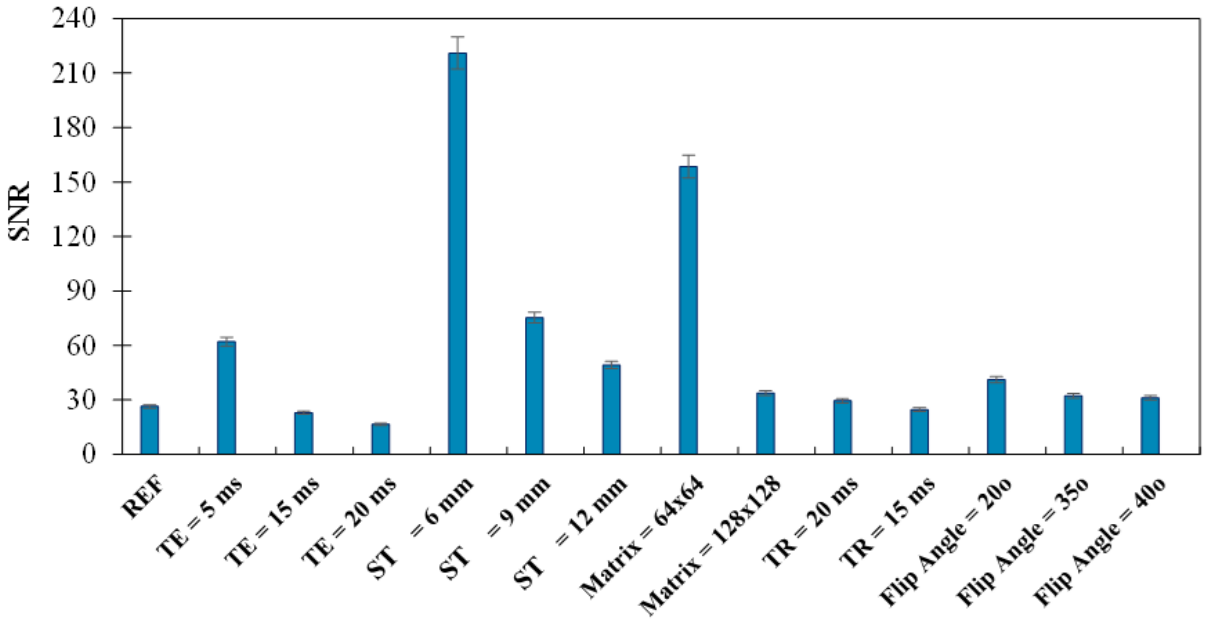

***Figure 11**: Graph that shows SNR for different sequence parameters.*

A slice thickness of 6 mm, with a TR of 25 ms, TE of 10 ms, 96x96 resolution, and a FA of 30°, resulted in the highest SNR, indicating that this configuration provides the most reliable imaging results and was therefore used for subsequent experiments.

3.1.2 Calculation of PRF Coefficient for Agar-Silica Phantom

Figure 12 shows representative results from PRF coefficient estimation for the optimized phantom recipe of 6% agar and 4% silica. **Figure 12A** compares the focal temperature profiles from thermocouple measurements in the lab (blue line) and PRF-based MR thermometry using the typical PRF coefficient for humans (orange line) for sonication at an electric/acoustic power of 100/30 W for 60 s, at a FD of 3 cm. In the same graph, the fitted curve (green line) with a PRF coefficient (α) value, calibrated to best align with the temperature profile from the thermocouple measurements, is shown. The corresponding temperature coefficient is -0.0054 ppm/°C. **Figure 12**B and **Figure 12**C show temperature and thermal dose maps generated with the calculated PRF shift coefficient, respectively.

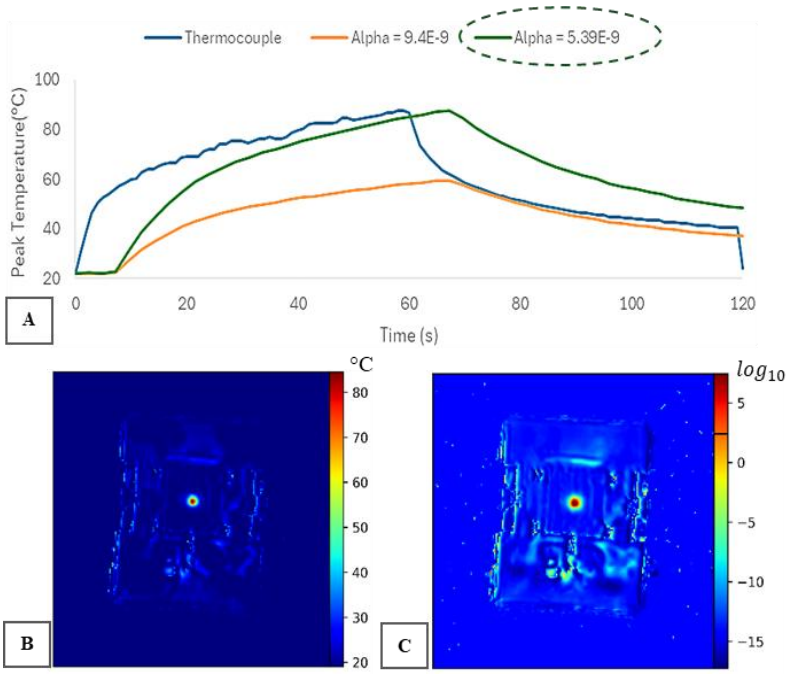

***Figure 12**: (A) Focal temperature evolution during and after sonication (100 W, 60 s), measured using both a thermocouple and MR thermometry. (B) Thermal map at the end of sonication, calculated using the derived α coefficient. (C) Corresponding thermal dose map.*

3.2 Thermal Effects of FUS in Agar-Silica Phantoms

3.2.1 Threshold for effective lesion creation

Figure 13 displays a series of T2-W images of the phantom obtained after sonications with the 1 MHz transducer at increasing power levels, while keeping the sonication time at 20 s. These images reveal lesion development, initially indicated at 39 W and becoming apparent at 42 W.

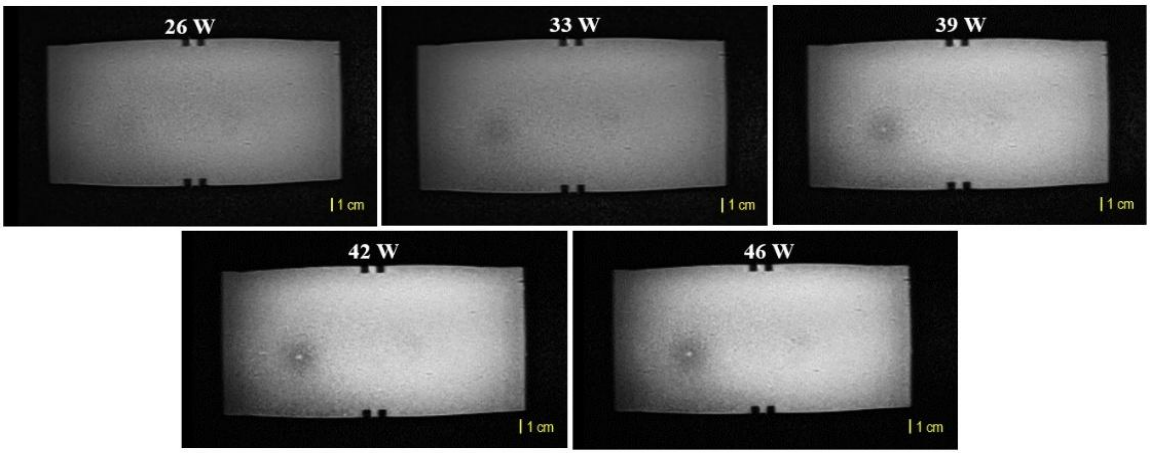

***Figure 13**: T2-W TSE coronal images of the phantom after sonication with transducer No. 3 (1 MHz) at varying acoustic power levels (26–46 W, corresponding to focal intensities of 600–1050 W/cm²) with a constant sonication duration of 20 s.*

Therefore, the minimum acoustic power required to create a lesion with accurately measurable dimensions was determined to be 42 W (focal intensity of ~970 W/cm²). The resulting lesion had a diameter of about 2.5 mm, thus meeting the authors' criterion of being at least 4 pixels in

size. This suggests a minimum focal temperature of 39 °C for effective lesion creation, which translates to a threshold accumulated thermal dose of 1.49 x 10^{-4} CEM43°C.

3.2.2 Repeatability of Phantom's Thermal Response

Figure 14 shows the superimposed focal temperature profiles from the repeatability test of five identical sonications (150/45 W electric/acoustic power, 60 s, FD of 3 cm) performed in the agar/silica phantom with transducer No.1 (2.75 MHz). The mean temperature change observed from these measurements was 38.5 ± 2.1 °C, with a 95% confidence interval estimated to be between 37.2 and 39.7 °C. The indicative thermal dose maps (expressed in logarithmic scale) for sonications 1 and 3, shown in the figure, reveal accumulated doses of 7.2 × 10^6 CEM43°C and 8.7 × 10^5 CEM43°C, respectively, both well above the necrosis threshold of 240 CEM43°C, as indicated by the black line on the scale.

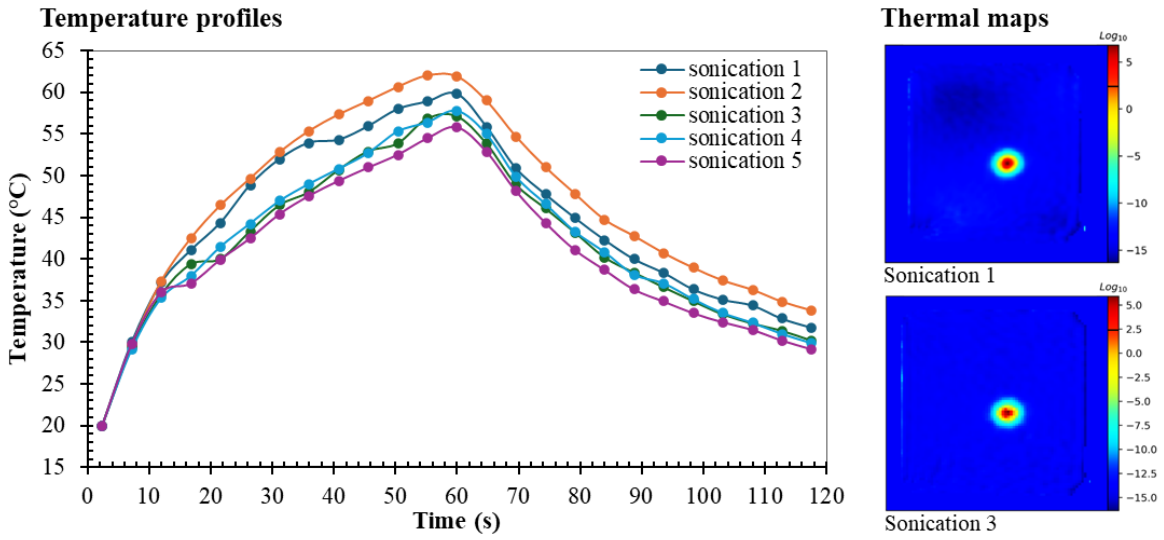

***Figure 14:**: Thermal profiles of five identical sonications performed in the agar/silica phantom using 45 W for 60 s at a FD of 3 cm (transducer No.1), along with corresponding coronal thermal maps.*

3.2.3 Thermal Mapping and Lesion Detection by MRI

Typical thermometry results from sonications in the plain agar-silica phantom (6% w/v agar, 4% w/v silica) are shown below, illustrating its response to FUS heating. **Figure 15** presents the focal thermal profile during a 60-s sonication at 97 W (FD of 3 cm) with transducer No.1 (2.75 MHz), revealing a temperature increase of 50 °C from a baseline of 19 °C. It also includes the corresponding temperature and thermal dose maps extracted from the software for both the coronal and axial planes, along with post-sonication T2-W TSE images that clearly show the formed lesion as a hyperintense area.

Complementary to this, **Figure 16** highlights the significance of silica inclusion by comparing lesion manifestation on T2-W images between an agar-only phantom and a silica-doped phantom with identical agar content. In this case, both gels were exposed to 100 W for 90 s. Note that no lesion was visible in the agar-only gel, while the silica-doped gel exhibited a high-contrast white lesion.

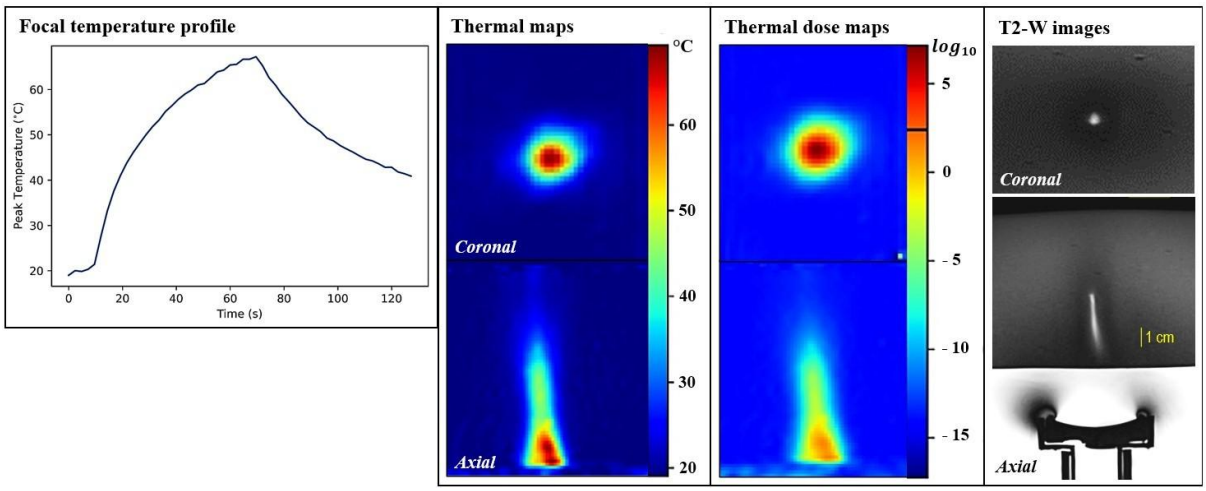

***Figure 15**: Focal temperature profile during and after sonication (97 W, 60 s), along with relevant coronal and axial temperature maps, thermal dose maps (black bar indicates a thermal dose of 240 CEM43°C) and post-sonication T2-W TSE images showing the lesion as an area of increased intensity.*

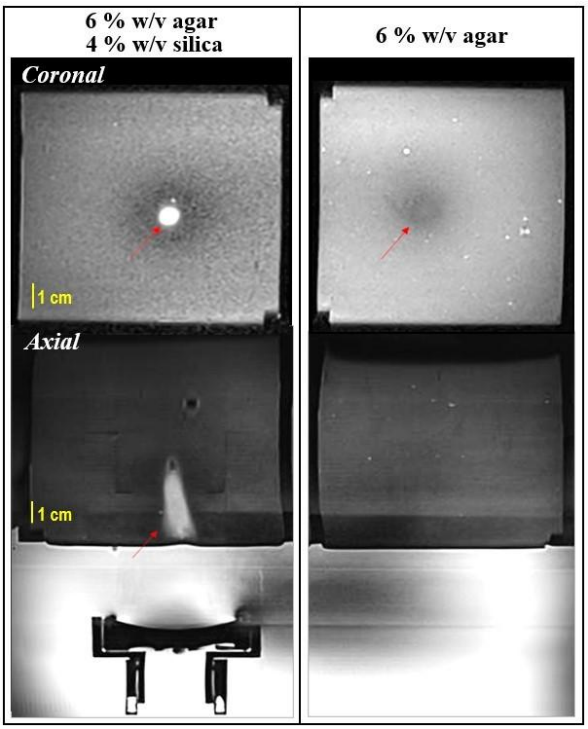

***Figure 16**: Comparison of coronal and axial post-sonication (100 W, 90 s) T2-W TSE images between a pure agar gel and a silica-doped one with identical w/v agar concentration of 6%.*

Figure 17 presents an example of coronal thermal mapping, showing the temperature distribution and accumulated thermal dose resulting from a lower-power sonication (electric/acoustic power = 150/ 45 W) using transducer No.3 (1 MHz) for similar duration (60 s) deeper in the phantom (FD = 35 mm).

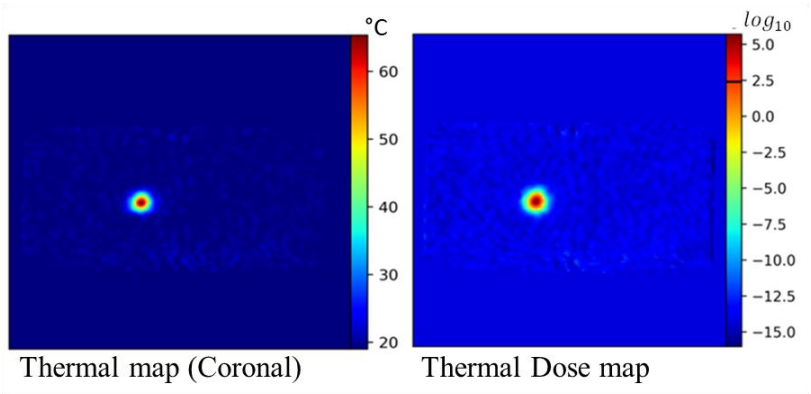

***Figure 17**: Temperature and thermal dose maps produced upon completion of sonication in the 6% w/v agar, 4% w/v silica phantom (Electric/ Acoustic Power = 150/ 45 W for 60 s, FD of 35 mm, transducer No.3).*

A representative example of a robotic-assisted grid sonication in this phantom model (6% w/v agar, 4% w/v silica) is presented in **Figure 18.** Sonication was carried out with transducer No.1 (2.75 MHz) with the following parameters: grid size of 4×4, motion step of 3 mm, cooling time of 60 s, electric/acoustic power of 250/75 W, sonication time of 60 s, and a FD of 25 mm. The thermal dose map indicates values exceeding the threshold for tissue necrosis, marked by the black line on the unit bar (**Figure 18B**), which aligns well with the predicted necrotic area (**Figure 18C**). A highly hyperintense lesion was observed on the corresponding T2-W TSE images. The coronal view (**Figure 18D**) shows a centrally located, round-to-oval hyperintense lesion, while the axial view (**Figure 18E**) reveals a vertically oriented, columnar (cigar-shaped) lesion. A photo of the phantom revealing the inflicted lesion is shown in **Figure 19**.

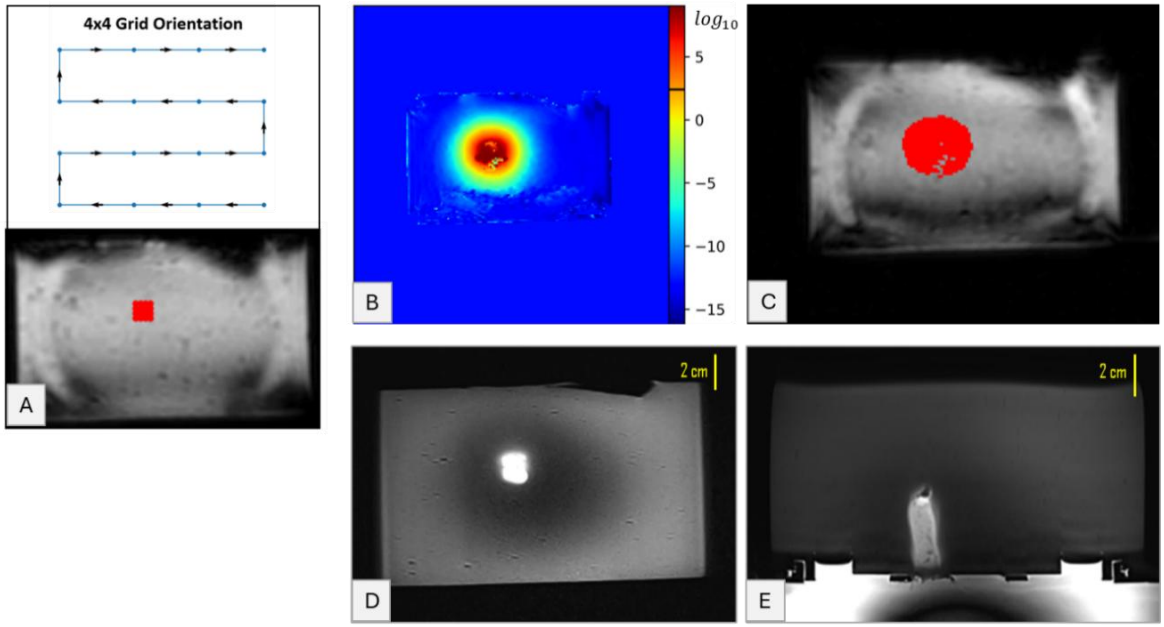

***Figure 18:** A) Sonication grid as planned on reference phantom image and Sonication pattern. B) Colour-coded thermal dose maps after completion of the sonication grid (4x4, 3 mm step, 75 W ac. power, 60 s on/off time). C) Simulated necrosis area after completion of the sonication grid. D) Post-sonication T2-W TSE Coronal image, revealing inflicted lesion in a plane perpendicular to the beam direction. E) Corresponding Axial T2-W TSE image, revealing the inflicted lesion at a plane parallel to the beam direction.*

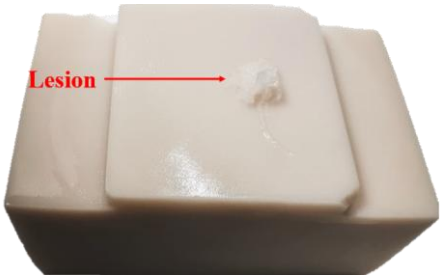

Figure 19: *Photo of the phantom following completion of sonication, revealing the inflicted lesion on the phantom's sonicated surface.*

3.2.3.1 Effect of sonication parameters on lesion dynamics

Figure 20A illustrates indicative results of varying sonication power and time on lesion formation for transducer No.1 (2.7 MHz). Acoustic powers of 75 W (corresponding to a focal intensity of 17,600 W/cm²) and 90 W (approximately 21,100 W/cm²) were tested, with sonication times ranging from 5 to 20 s in 5-s intervals. These outcomes suggest that at least 90 W of acoustic power is required to create a clearly visible lesion with measurable dimensions (> 2 mm) within 5 s at a FD of 23 mm. Axial images revealed cigar-shaped thermal lesions with increased visibility (enhanced contrast) as the applied ultrasonic energy was increased (either through increased power or time).

Similarly, **Figure 20B** illustrates how lesion size increases as the exposure duration at a similar power of 75 W extends from 10 to 70 s, using transducer No.3 (1 MHz, small diameter) set to a FD of 35 mm. Due to its weaker focusing, the corresponding focal intensity is 1590 W/cm². Note that compared to transducer No.1 lesions became less uniform, with their diameter increasing towards the transducer, and this effect intensified as exposure time increased.

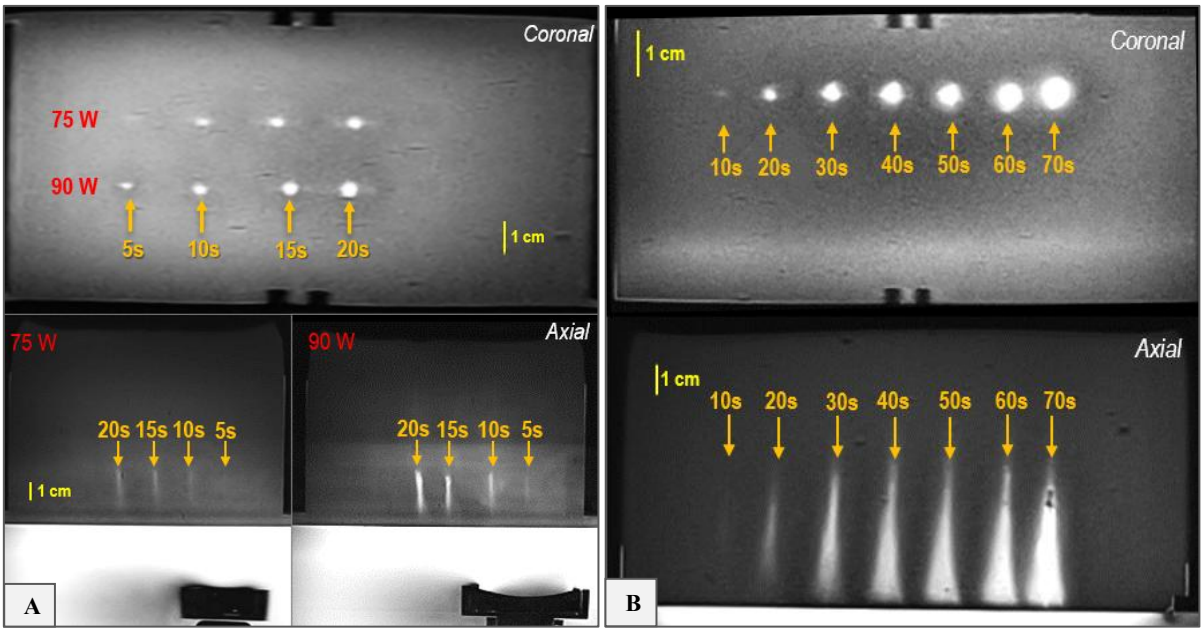

Figure 20*: A) Coronal and Axial T2-W TSE images of the phantom following sonications at 75 and 90 W acoustic power for 5-20 s at FD of 23 mm (transducer No.1), showing inflicted lesions. B) Coronal and Axial T2-W TSE images of the phantom following sonications at 75 W for 10-70 s at a FD of 35 mm (transducer No.3), showing inflicted lesions.*

These observations are further supported by the quantitative data in **Figure 21**, which also reveal that lesion length plateaus after 40 s.

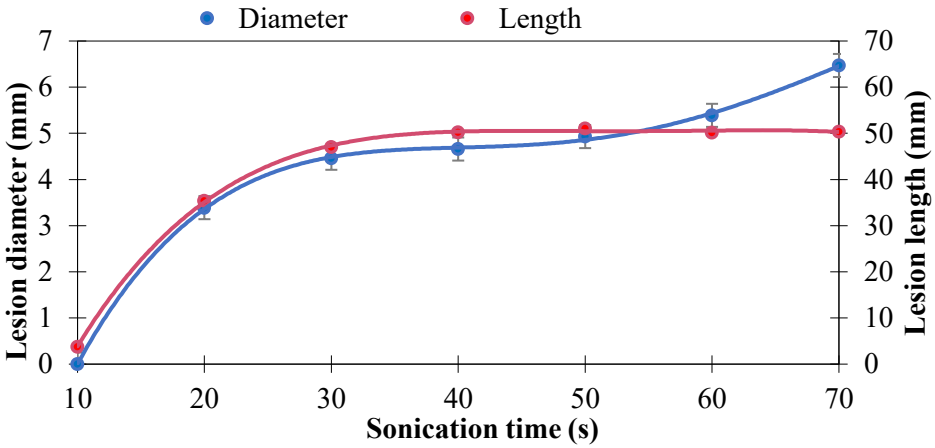

***Figure 21**: Lesion diameter and length versus sonication time for sonication at 75 W for 10-70 s at FD of 35 mm (transducer No.3, 1 MHz).*

Transducer No. 2 was employed to investigate deep-tissue targeting, owing to its larger radius of curvature (focal distance). This transducer enabled precise focusing at depths of up to 70 mm, consistently producing elongated, cigar-shaped lesions deep within the phantom (6 % w/v agar, 4 % w/v silica). A representative result is shown in **Figure 22**, which illustrates a 1×3 lesion grid formed at approximately 20 mm spacing, using the manual setup. The sonications were performed with an electric/acoustic power of 400/ 120 W, with sonication durations of 20, 30, and 40 s.

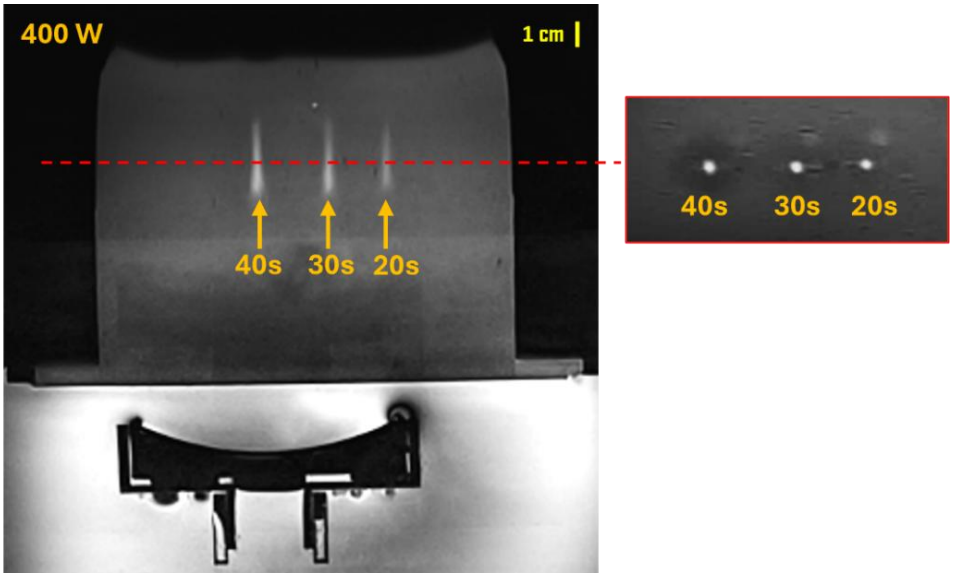

***Figure 22:** Coronal T2-W TSE image of agar-based phantom acquired after grid sonication with varied sonication time showing inflicted lesions. Figure 13: Axial T2-W TSE image of agar-based phantom acquired after grid sonication (400 W) with varied sonication time showing inflicted lesions (red arrows).*

3.2.3.2 Regression of lesions over time

In comparing T1-W and T2-W TSE imaging, the maximum CNR between the formed lesion and the surrounding agar gel was 350 with T2-W imaging; significantly higher than the maximum CNR of 40 achieved with T1-W imaging. **Figure 23** displays representative

regression patterns of lesions induced by exposure to 120 W acoustic power (focal intensity of 6400 W/cm2) for 30 s utilizing transducer No.2 (1 MHz, large diameter). The normalized CNR changes over the 15-min observation period are presented graphically, with the time of the first image acquisition designated as time zero. The CNR in T2-W TSE images decreased rapidly, dropping to approximately 10% of the initial CNR within 6 minutes. In contrast, during the same period, T1-W TSE images maintained 35% of the maximum post-sonication CNR, with lesion disappearance at about 14 min. Note that T1-W imaging reached maximum lesion contrast a few minutes after completion of sonication. Overall, due to its superior CNR, rapid lesion regression (essential for reusability), and ability to capture peak CNR immediately after sonication, the employed T2-W sequence was selected for subsequent experiments. T2-W images acquired at different time points after completion of sonication are shown in **Figure 24**. Note that complete resolution of the lesion was achieved after 15 minutes.

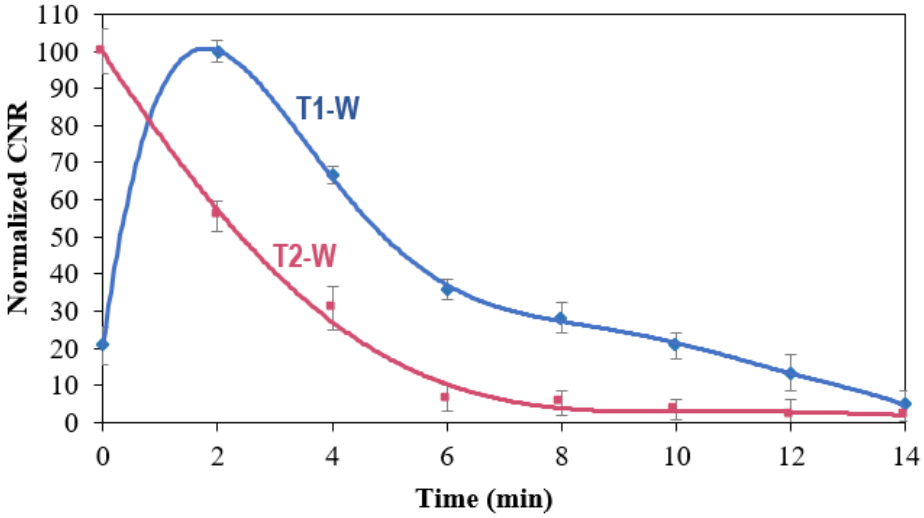

Figure 23: *Normalized CNR of lesion on T1-W and T2-W images plotted against post-sonication time (120 W ac. power for 30 s with transducer No.2)*

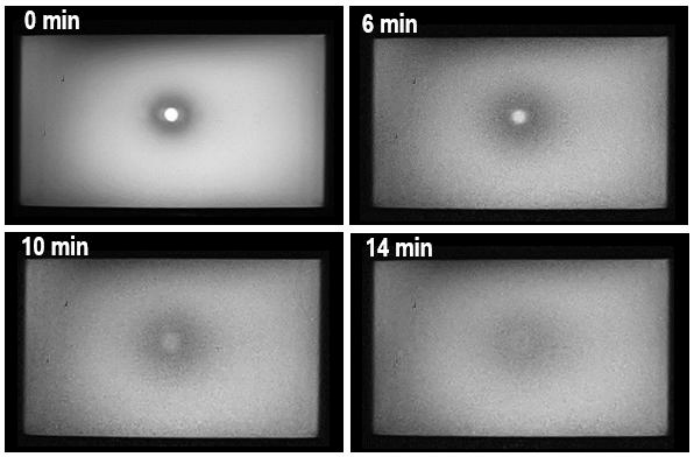

Figure 24: *A) T2-W images acquired at different time points after completion of sonication at 120 W ac. power for 30 s (transducer No.2).*

Further confirmation of these findings is provided by the T2-W TSE coronal images displayed in **Figure 25**. As observed, lesion disappearance occurred around 15 minutes post-sonication, following the application of an electric/acoustic power of 300/100 W, for 90 s at a FD of 30 mm, using Transducer No. 1 (2.75 MHz).

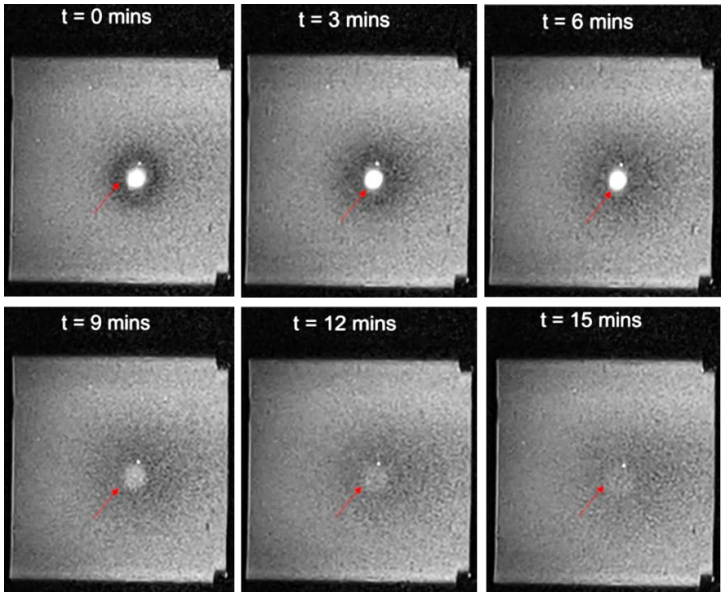

Figure 25: *A) Coronal T2-W TSE images of the phantom acquired every 3 minutes after sonication (ac. power of 100 W, 90 s at a FD of 30 mm) showing thermal heating at the focal spot (red arrow).*

3.3 Phantom Vs Excised Porcine Tissue: Thermal Response and Lesion Formation

Figure 26 compares the outcomes of an 8x8 grid sonication (5 mm step size) conducted on both the agar-silica phantom and excised porcine tissue sample using transducer No.1. In each case, 90 W acoustic power were applied for 30 s at each point, with a 60-s delay between sonications, and a FD of 3 cm. The sonication pattern followed a zig zag trajectory initiating from the bottom-right corner and proceeding in alternating directions along each row throughout the grid. The thermal dose maps showed a strong correlation with the corresponding lesion patterns observed in the phantom and tissue, confirming that thermal doses exceeded the necrotic threshold.

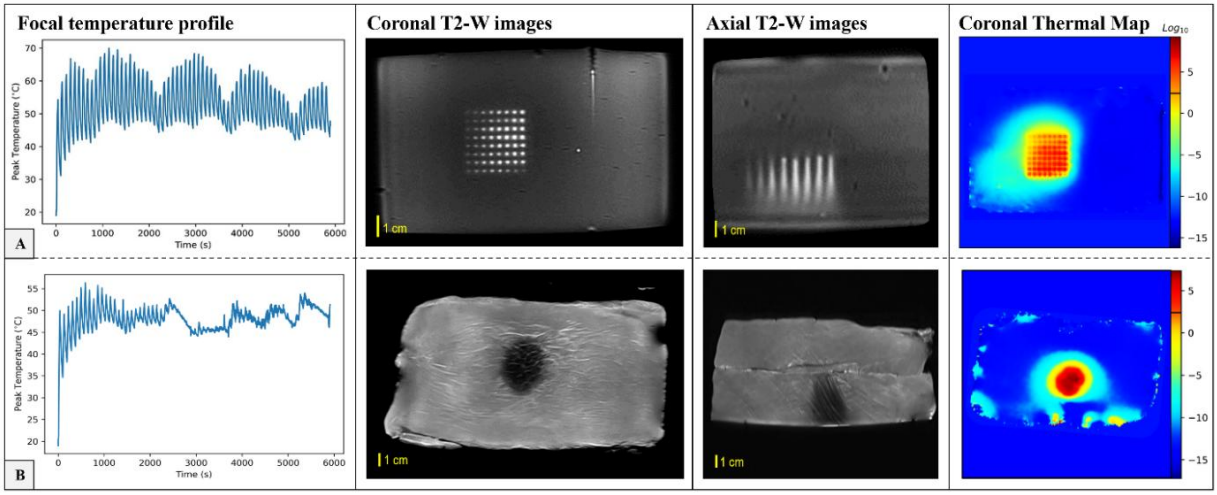

Figure 26: *Focal temperature profile, presented as a time-series graph of temperature evolution at the various sonication points, along with post-sonication T2-W TSE coronal and axial images, and coronal thermal dose maps (8x8 grid, 5 mm step, 90 W, 30 s on time, 60 s delay) for the A) Agar/silica phantom and B) Porcine tissue.*

3.4 Near field heating

Figure 27 presents a series of post-sonication axial T2-W TSE images for a 1×8 grid with a 4 mm step size, using acoustic power of 90 W. The images illustrate how varying sonication durations and inter-sonication delay intervals influence lesion formation, including lesion overlap, discreteness, and the extent of thermal effects. All images show heat diffusion extending toward the lesion tail, resulting in a confluent area of hyperintensity where individual lesions can no longer be distinguished. A 60-second delay was generally the minimum needed to generate discrete lesions at the given acoustic power and spatial step, with distinct foci visible in the upper lesion regions. This was further confirmed by coronal (cross-sectional) images showing distinct lesion separation. However, the diffusion phenomena observed at the lesion tail and overall lesion dynamics were found to be highly dependent on the specific transducer used, aligning with the observations described in Section 2.3.3.

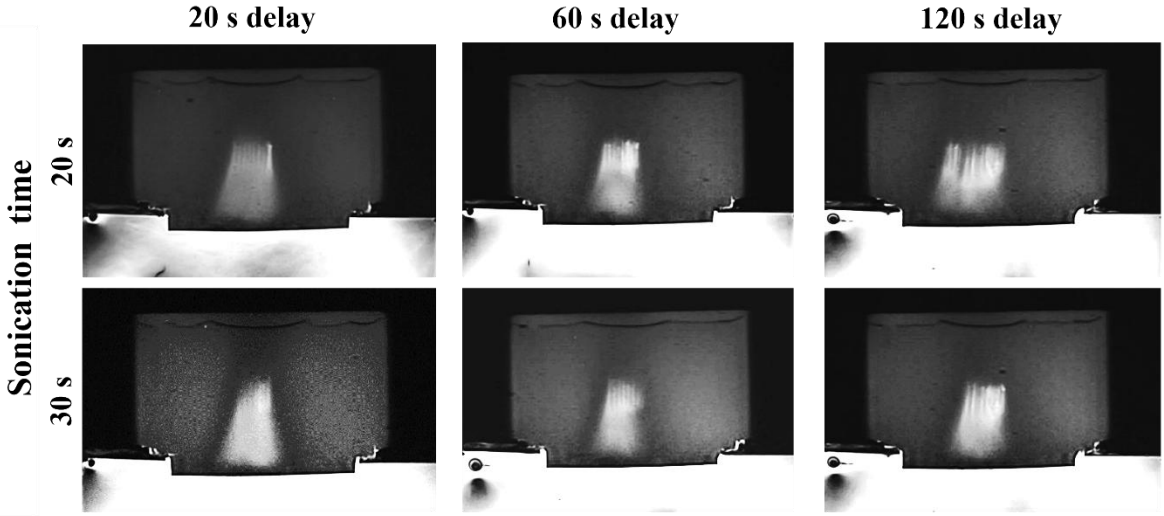

***Figure 27**: Axial T2-W TSE images of the phantom acquired after the execution of grid sonications with acoustic power of 90 W, varying sonication time and delay, at a FD of 50 mm.*

3.5 Tumor phantom model: MRI assessment of Thermal effects and Lesion formation

Indicative results from FUS sonications in a tumor phantom model of simple rectangular design using transducer No. 4 are shown in **Figure 28**. These results were obtained using the highest tested electric/acoustic power of 400/100 W and a sonication time of 60 s.

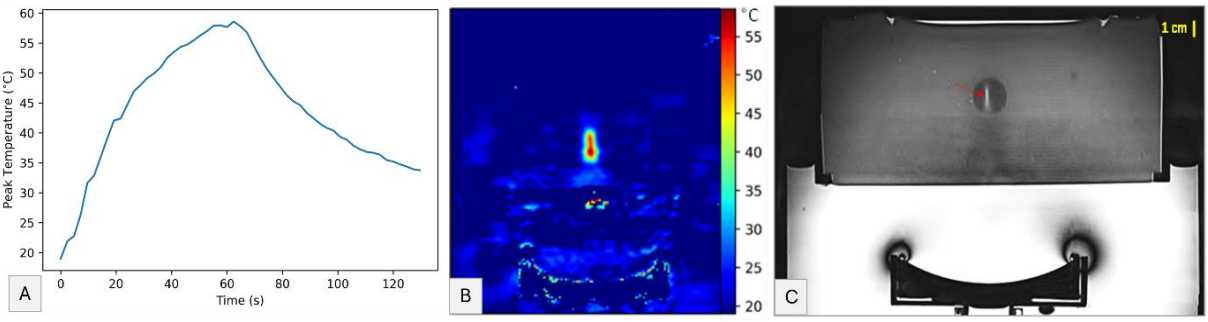

***Figure 28:** A) Focal temperature change within tumor mimic during and after sonication (400 W, 60 S). B) Corresponding axial colour-coded thermal map produced upon completion of sonication. C) Axial T2-W TSE image of the phantom acquired after completion of sonication in the tumor mimic, revealing the inflicted lesion (red arrow) at a plane parallel to the beam direction.*

Figure 28A presents the focal temperature profile recorded in the tumor mimic (6% w/v agar & 6% w/v silica, 2 cm diameter) during and shortly after sonication at a FD of 45 mm. The corresponding thermal map at the end of the sonication is shown in **Figure 28B**, while **Figure 28C** depicts the formed lesion on a T2-W TSE image acquired post-sonication. At the highest applied power (400 W for 60 s), the maximum temperature rise (ΔT) in the background phantom material (6 % w/v agar & 2 % w/v silica) was 25.5 °C, whereas the tumor mimic exhibited a substantially higher ΔT of 39.6 °C (Peak Temperature of 58.6 °C). This difference is attributed to the increased ultrasonic absorption of the tumor-mimicking composition (owning to higher silica concentration), resulting in greater localized heating.

3.6 Flow phantom

3.6.1 Evaluation of Imaging Features

Both MRI and CT scans revealed the water-filled flow channels, as illustrated in **Figure 29**. T2-W TSE imaging depicted the channels as hyperintense regions, contrasting with the surrounding greyish phantom material. Sequential coronal images revealed different sections of the tubing network (**Figure 29A)**, while axial images allowed visualization of the transducer's position relative to the phantom and confirmed the accurate placement of the focal spot (**Figure 29B**). In CT imaging, the vessel cross-sections appeared as hypointense spots (**Figure 29C**).

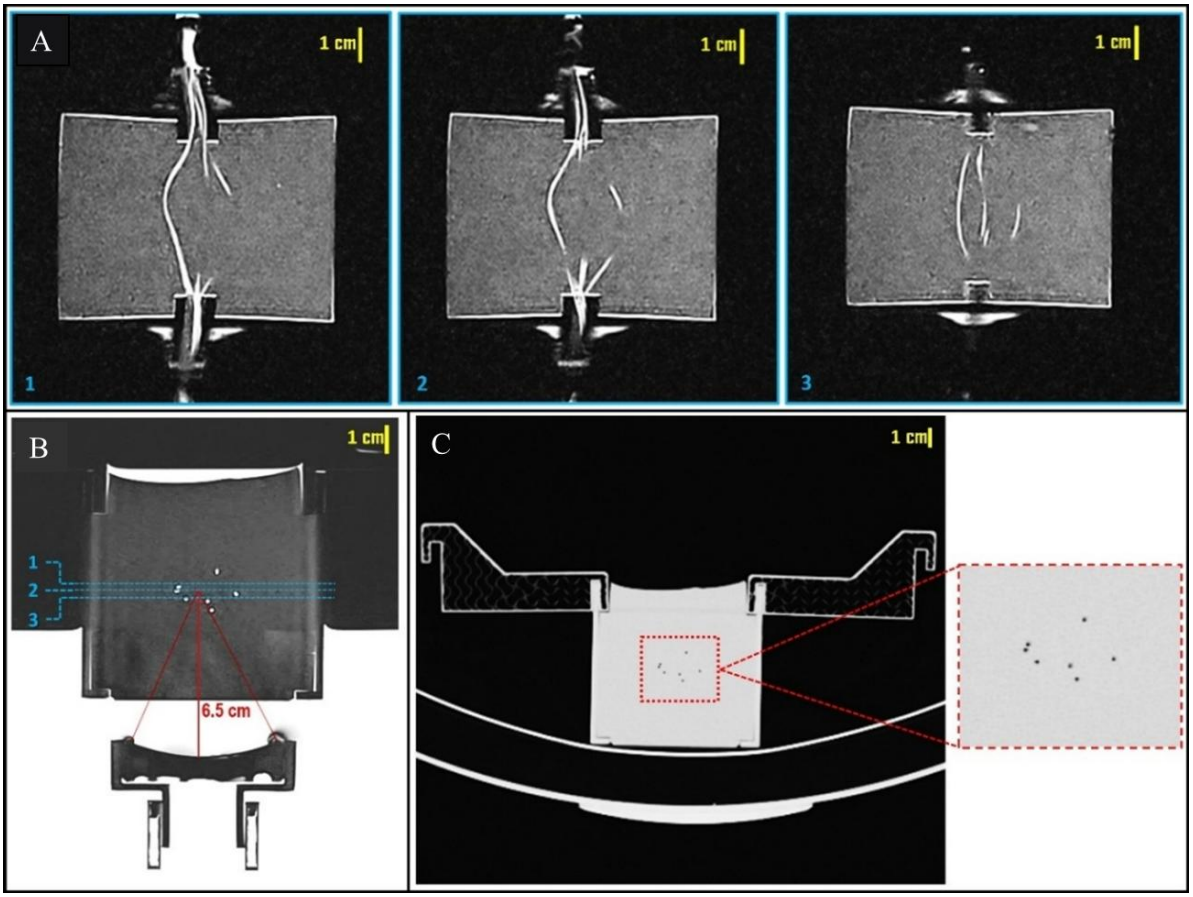

Figure 29*: A) T2-W TSE coronal images of the flow phantom (1.5-mm sequential slices). B) T2-W TSE axial image of the flow phantom, with red lines indicating the focal depth and blue lines the location of each coronal slice (1 to 3). C) CT image of the flow phantom.*

3.6.2 Evaluation of Thermal response

The phantom's thermal response to increasing applied power was consistent with expectations. **Figure 30** shows coronal thermal maps, acquired as cross-sections at the focal point, upon reaching 30 s of sonication at 15, 30, and 45 W. These maps illustrate temperature distribution in the relevant plane, demonstrating a slight expansion of the heated area alongside increasing temperature, as also reflected in the corresponding temperature profile graph.

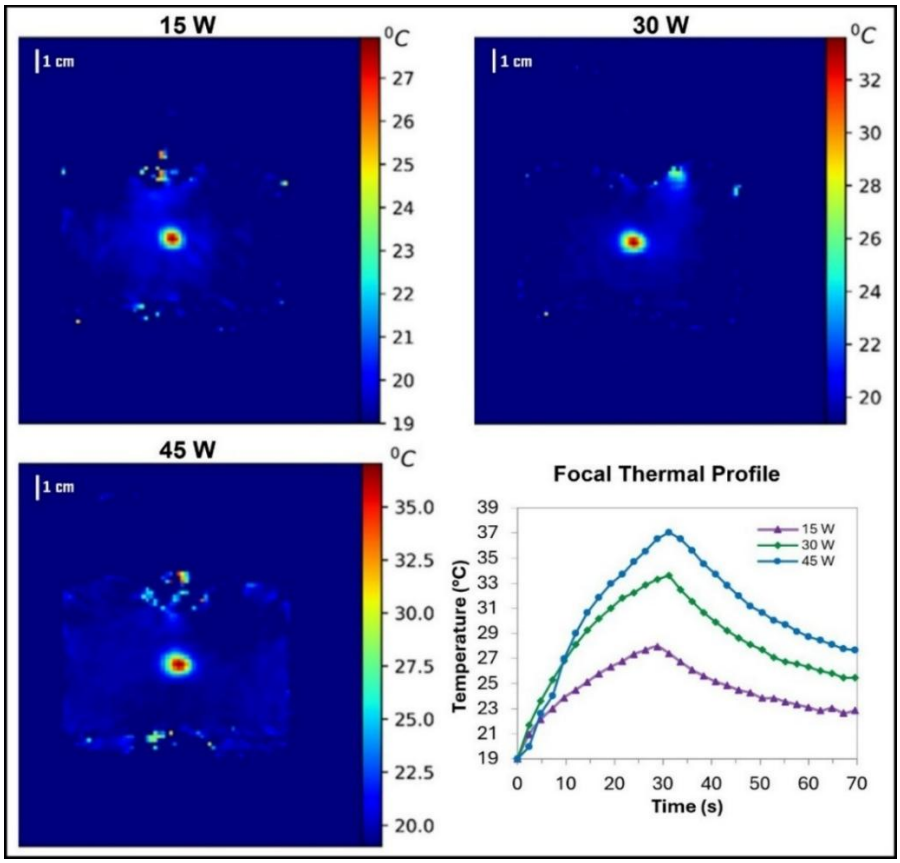

***Figure 30**: Colour-coded coronal thermal maps following sonication in the flow phantom at varied acoustic power and constant duration of 30 s, along with corresponding focal thermal profiles.*

Intriguing behaviour was observed in the axial thermal mapping. **Figure 31** presents axial temperature maps from flow phantom sonication at two energy levels, compared to maps from the static phantom under similar conditions. When applying 15 W for 60 s (900 J), a slight downward shift of about 1.5 mm in the focal point was observed in the flow phantom, compared to the static condition. Except from this minimal shift, elevated temperatures were observed, spreading over a wider region compared to the static (no vessel) phantom. Increasing the power to 45 W for 30 s (1350 J) caused a significant downward shift of 10.5 mm, along with a noticeable rise in temperatures in the flow phantom compared to the static phantom. Once again, beam deformation was observed, resulting in a triangular heating pattern directed towards the bottom of the phantom. Overall, maximum recorded temperatures were approximately 25% higher in the flow phantom. It is, though, interesting to note that when examining the intended focal depth (consistent with the focal point location in the static phantom), slightly lower temperatures were recorded in the flow phantom, as shown in the temperature profile graphs.

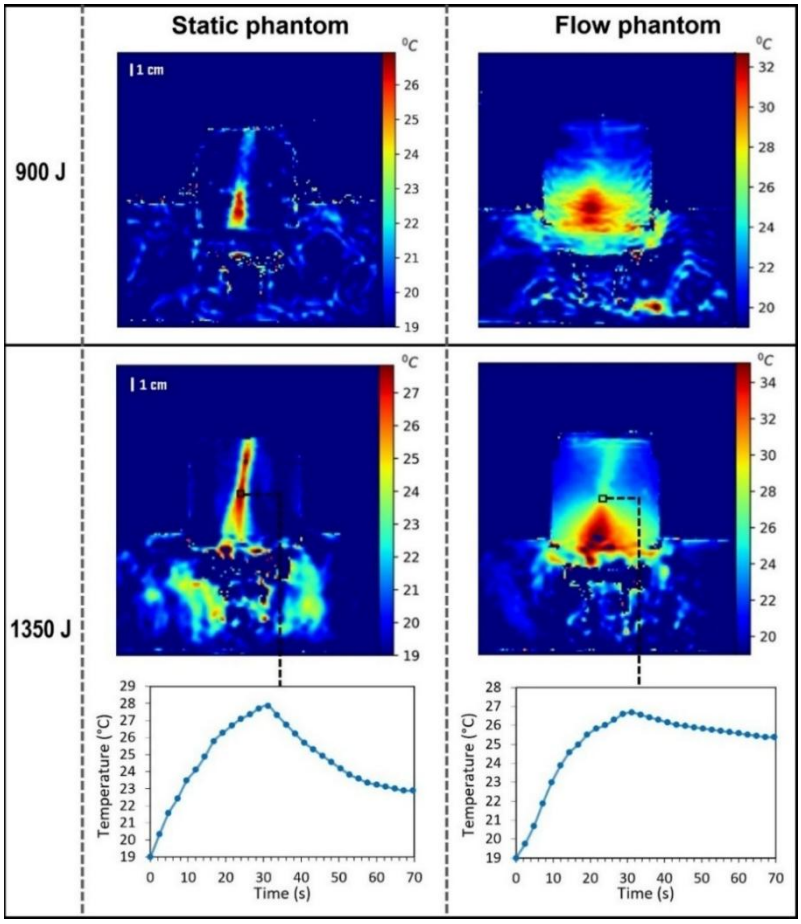

***Figure 31**: Color-coded axial thermal maps following sonication in static and flow phantoms at two different ultrasonic energy levels, along with temperature profiles at the intended focal depth (marked by the small black rectangular box) for the higher energy level (1350 J).*

3.7 Head phantom model with tumor simulators

3.7.1 Single and grid sonications: Effect of sonication parameters

Figure 32 displays typical thermal maps obtained from high-power exposure targeting the tumor mimic without skull obstruction, using 120 W acoustic power (focal intensity of 6397 W/cm^2) for 40 s, at a FD of 70 mm, along with the corresponding focal temperature evolution. Notably, the large radius of curvature (100 mm) transducer operating at 1 MHz (No.2) was employed to achieve focusing at this depth.

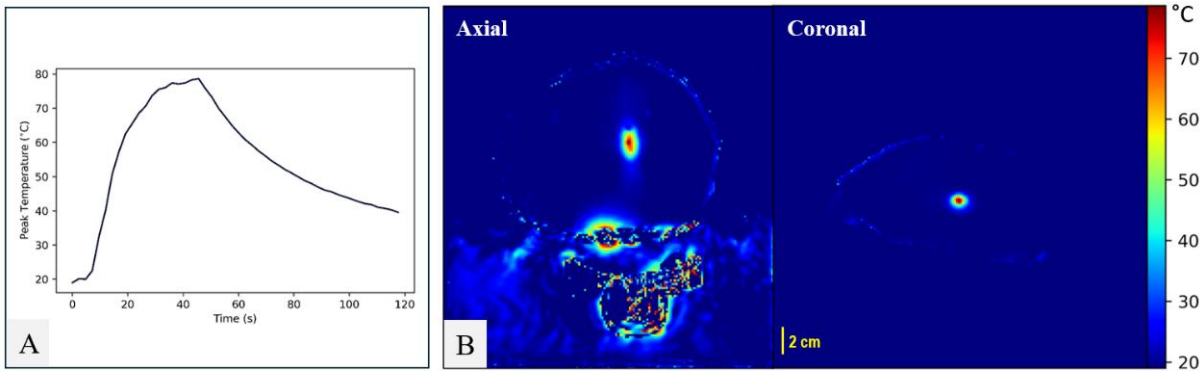

***Figure 32**: (A) Focal temperature profile during and after a 40-s sonication at 120 W (6397 W/cm^2). (B) Corresponding thermal maps showing temperature distribution within the tumor.*

An indicative example of the characteristic appearance of thermal lesions in the proposed phantom is illustrated in **Figure 33**. In this case, an electric/acoustic power of 350/105 W (focal intensity of 5597 W/cm²) was applied to a 3-cm tumor mimic for 40 s at a FD of 50 mm, using the transducer No.2 (1.1 MHz), without skull interference. The resulting lesion exhibited significantly increased intensity and well-defined borders on post sonication T2-W TSE images. It is important to note that the right lower part of the tumor was intentionally selected as the target during planning on reference coronal images.

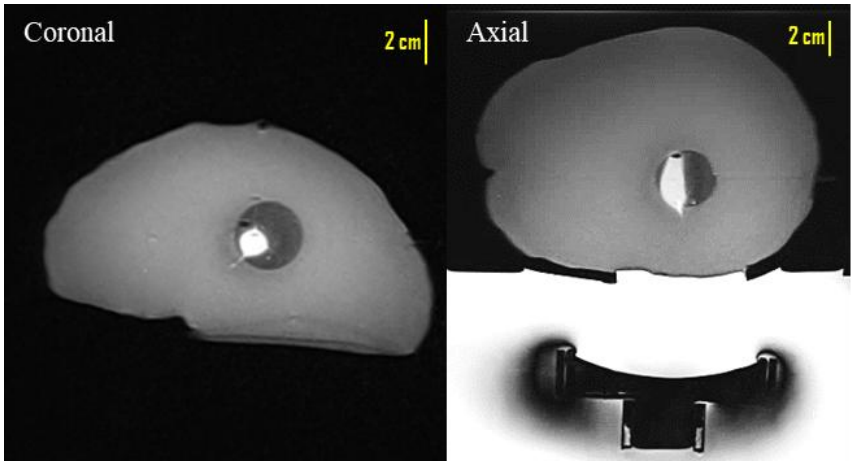

Figure 33: *T2-W TSE images of the phantom showing the thermal lesion formed within the tumor from exposure at 105 W (5597 W/cm²) for 40 s at a FD of 50 mm.*

In **Figure 34**, the lesion that had nearly covered the tumor mimic after sonication at 200/ 64 W electric/ acoustic power for 60 s with transducer No. 3 (1 MHz) is shown to have completely disappeared on the T2-W image taken 17 minutes later, following its gradual dissipation as seen in the previous intermediate image.

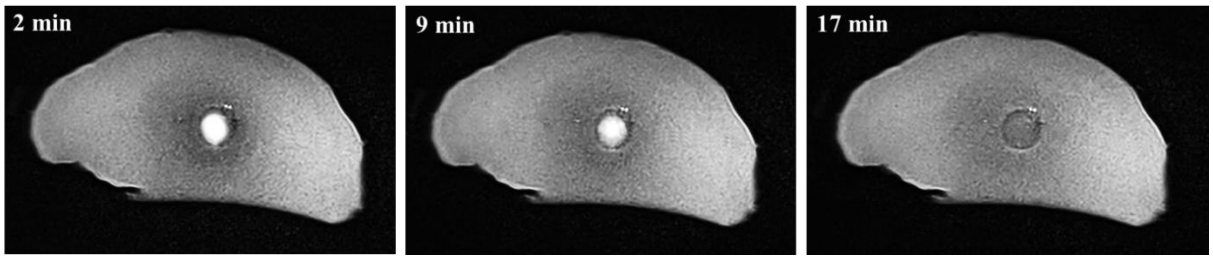

Figure 34: *Coronal T2-W TSE images of the phantom acquired 2-, 9-, and 17-min after completion of sonication in the tumor mimic at 64 W ac. power for 60 s, revealing the inflicted lesion at a plane perpendicular to the beam direction.*

Figure 35 shows grid sonication applied to a tumor-bearing head phantom, with a 2 cm tumor mimic placed 4.5 cm deep. The sonication was performed using transducer No. 3 (1 MHz) in a 5×5 grid pattern with a 4 mm step size, delivering 250/75 W of electric/acoustic power, with a 30-s sonication time and a 60-s delay between pulses. The entire tumor was successfully sonicated. Interestingly, grid points located just outside the tumor appeared discrete, due to lower ultrasonic absorption in the background material compared to the silica-doped tumor.

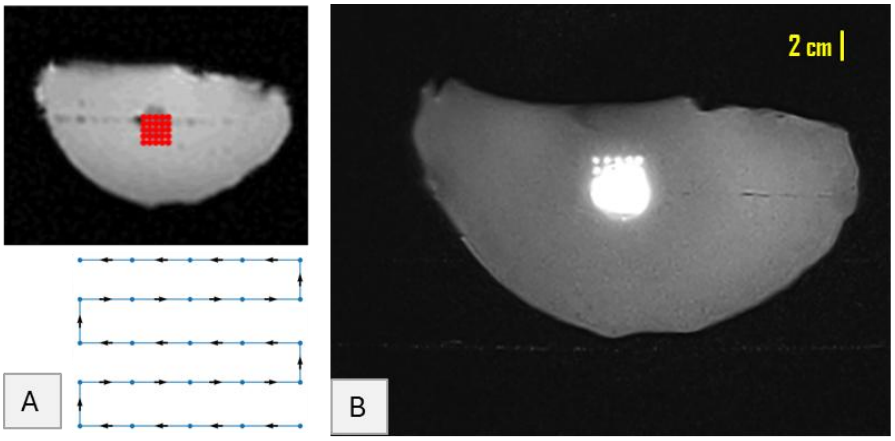

***Figure 35**: A) Treatment planning showing arrangement of the grid sonication points relative to the tumor mimic (top) and the order in which points were sonicated (bottom). B) Post-sonication T2-W TSE coronal image showing overlapping lesion covering the entire tumor.*

3.7.2 Beam Obstruction by Skull Mimic

3.7.2.1 Effect of different printing materials

Table 5 summarizes thermometry outcomes on the influence of incorporating skull mimics into the beam path on heat accumulation and resulting temperatures within the tumor. Specifically, it compares the maximum temperature and relevant change from a baseline of 19°C after sonication at acoustic power of 80 W for 30 s (FD of 35 mm) using transducer No.3 (1 MHz), between the unobstructed and skull-obstructed conditions. With this transducer, which has a focal beam area of 4.4 mm², 80 W corresponds to a focal intensity of 1838 W/cm². Additionally, the table includes attenuation coefficient values for the various polymers, which were sourced from prior literature,[12,13] highlighting their impact on FUS energy transmission.

***Table 5:** Maximum focal temperature (T_{max}) and corresponding temperature change (ΔT) from sonication at 80 W for 30 s at a FD of 35 mm in the presence of the different 1-mm thick skull mimics, along with their attenuation coefficient, compared to unobstructed sonication (No skull mimic).*

Skull mimic	T_{max} (°C)	ΔT (°C)	Attenuation (dB/cm-MHz)
Resin	69.7	50.7	4.2 ± 0.1 [13]
ASA	25.9	6.9	15.2 ± 1.6 [12]
TPU	21.3	2.3	23.1 ± 2.8 [12]
No skull mimic	84.1	65.1	N/A

These outcomes are further supported by the thermal maps in **Figure 36**, which compare thermal distribution in the phantom from sonications through ASA and resin skull mimics. The maps show how the focal area is distorted in the case of the ASA, whereas with the resin skull, accurate targeting is achieved with less noise in the image.

Note that since the resin skull had the least influence on focal temperature increase (20% lower increase compared to unobstructed sonication), allowing the generation of ablative temperatures in the tumor, it was selected for use in subsequent experiments.

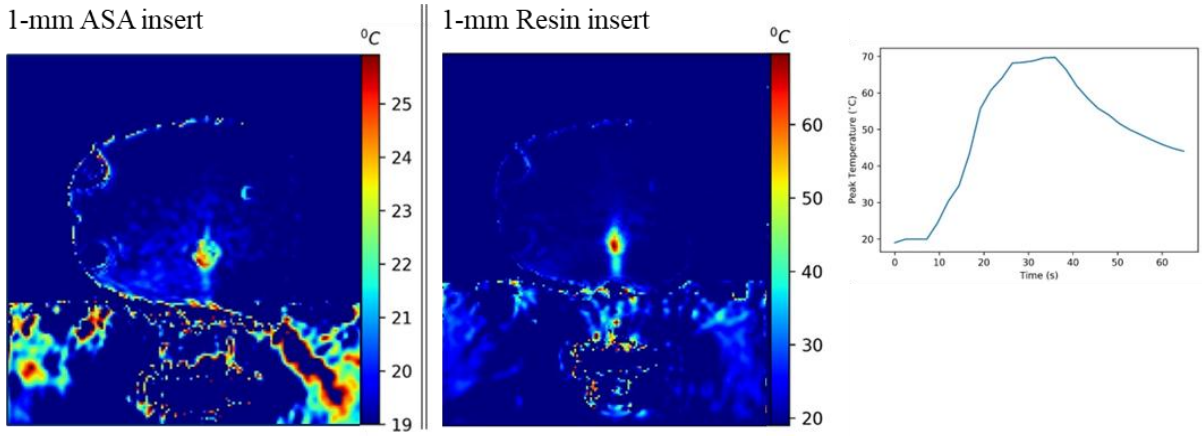

***Figure 36**: Colour-coded thermal maps produced upon completion of sonication in tumor mimic (250/80 W electric/acoustic power, 30 s, FD of 35 mm) through the 1-mm ASA and Resin skull mimics, along with the focal temperature change during and after sonication through the Resin skull mimic.*

Further results on the ability to efficiently sonicate the phantom through the 1-mm resin skull mimic are shown below. **Figure 37** presents a T2-W TSE image revealing the lesion resulting from sonication at 300/97.5 W electric/acoustic power for 60 s through the resin skull (FD = 20 mm) using transducer No. 3 (1 MHz) in a plain head phantom (no tumor mimics). Notably, heat diffusion at the lesion tail caused a triangular-shaped lesion, rather than the expected cigar shape, which reached the surface of the phantom (proximal to the sonicated site). A maximum temperature of approximately 75°C was recorded, reaching ablative temperatures.

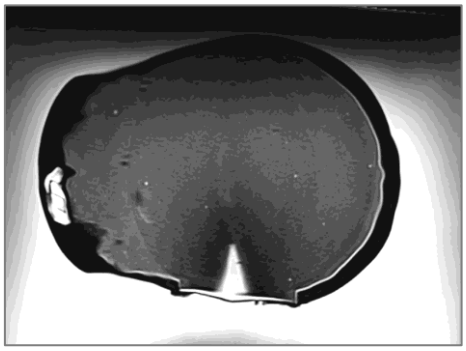

***Figure 37:** Axial T2-W TSE image of the head phantom following sonication (97.5 W ac. power, 60 s son. time, FD of 20 mm) through the 1-mm Resin skull mimic.*

Results on tumor ablation (2-cm tumor embedded at a depth of 4.5 cm) without a skull mimic are shown in **Figure 38A**, which shows a series of post-sonication T2-W TSE images of the phantom. In this experiment, a 2-cm diameter tumor was exposed to increasing ultrasonic energy using transducer No.3 (1 MHz) at a FD of 45 mm. Note that increasing the ultrasonic energy produced lesions of progressively larger dimensions. **Figure 38B** illustrates the thermal profile recorded for the highest applied energy of 2400 J (80 W for 30 s), demonstrating a maximum temperature of 73.6 °C (ΔT = 54.6 °C). For comparison, **Figure 38C** presents the corresponding T2-W TSE image obtained after sonication using the same parameters but with the 1-mm resin skull intervening in the beam path. The corresponding peak temperature recorded was 60.7 °C (ΔT = 41.7 °C), resulting in the formation of a thin, cigar shaped thermal lesion.

Despite the presence of the resin skull, a thin thermal lesion was formed in the tumor mimic without any off-target effects; smaller in dimension compared to the unobstructed field. Accordingly, the focal temperatures were significantly lower but still reached ablative levels.

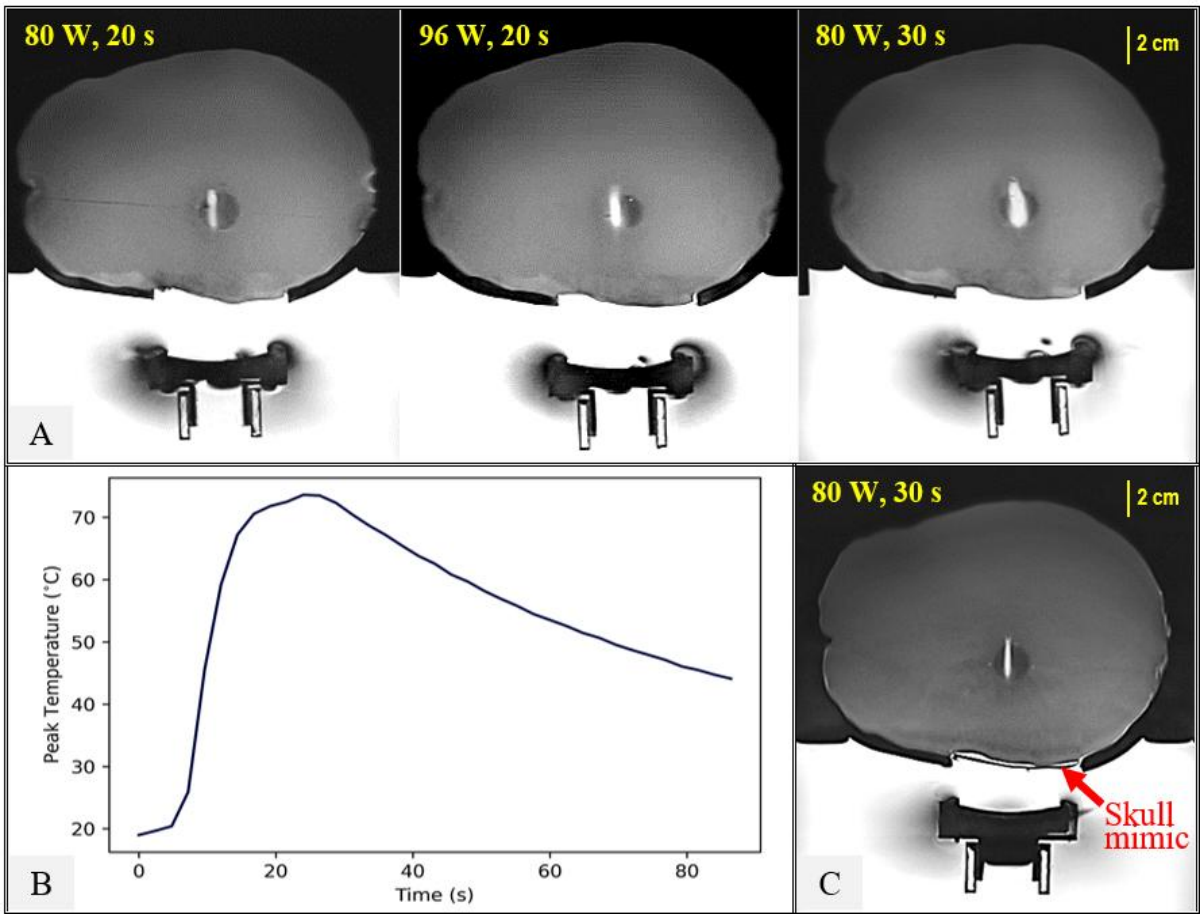

Figure 38: *(A) T2-W TSE images of the phantom after sonication of the tumor mimic at increasing acoustic energy levels (from left to right) without skull interference. (B) Focal temperature evolution recorded for the highest applied energy of 80 W for 30 s without a skull mimic. (C) T2-W TSE phantom image after tumor sonication through the resin skull.*

Similarly, **Figure 39** presents supplementary results in the form of thermal maps from sonications performed through the 1-mm resin skull mimic targeting the 2-cm tumor embedded at a depth of 4.5 cm. The first thermal map in **Figure 39A** corresponds to sonication using Transducer No. 3 (1 MHz) at 33 W acoustic power for 30 s. This is included for comparison with the second thermal map (**Figure 39B**), acquired under higher power conditions of 80 W for the same sonication time. These results demonstrate a logical thermal response, with induced temperatures increasing with applied ultrasonic energy.
Additionally, **Figure 39C** and **Figure 39D** includes coronal views of the resulting lesions (80 W, 30 s) acquired under resin skull-obstructed and unobstructed conditions, respectively, showing their cross-sectional diameter, corresponding to the axial images shown in **Figure 38A and Figure 38C**.

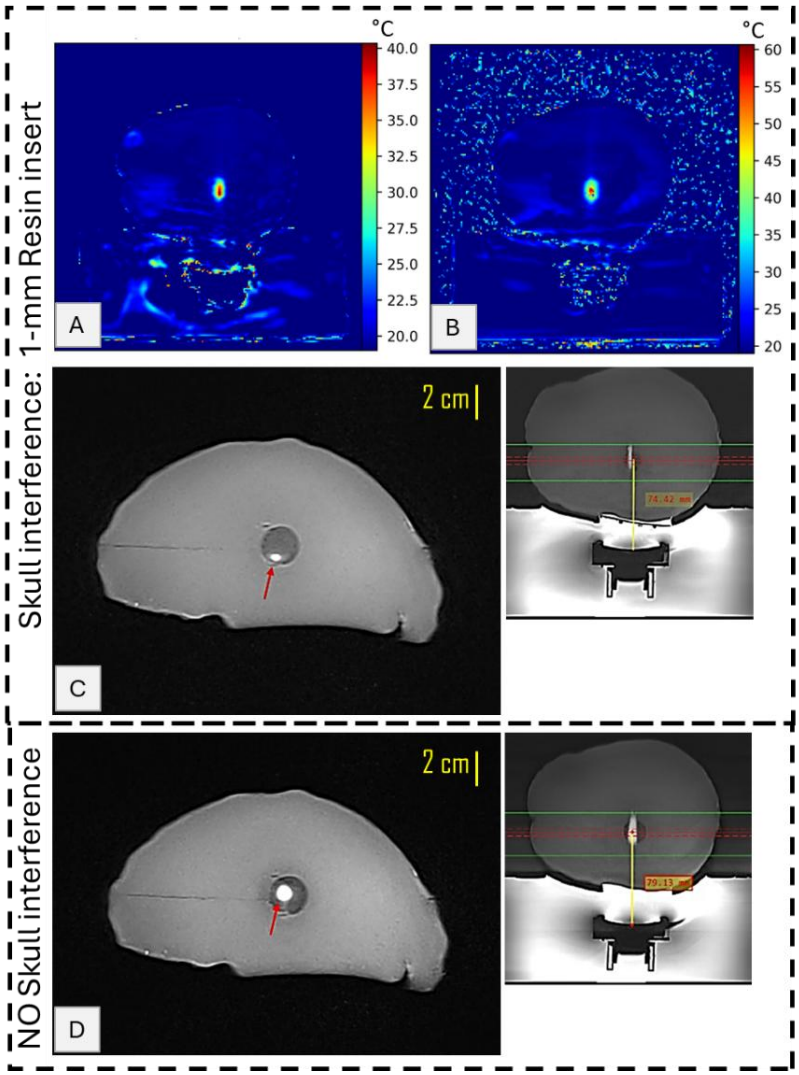

***Figure 39**: A) Axial thermal map after sonication in tumor mimic at ac. Power of 33 W for 30 s, at a FD of 4.5 cm through the 1-mm resin skull. B) Corresponding thermal map for ac. power of 80 W. C) T2-W TSE images acquired post-sonication (80 W, 30 s), revealing the inflicted lesion as an area of increased intensity at a plane perpendicular to the beam direction (red arrow shows the lesion). The axial image in the upper right corner indicates the location where the coronal slice was obtained. D) Corresponding T2-W TSE images acquired after sonication (80 W, 30 s) without skull interference.*

Figure 40 presents the outcomes of a 3x3 grid sonication (5-mm step) conducted on a 2-cm tumor mimic using the same transducer, without skull interference. An acoustic power of 80 W (1838 W/cm^2) was applied to each grid point for 60 s, leaving a 60-s cooling time (FD of 35 mm). In **Figure 40A**, the planned sonication pattern is overlaid on a FLASH image of the phantom, while **Figure 40B** shows the time series of focal temperature changes for all nine sonication points. The simulated necrosis map in **Figure 40C** aligns well with the lesion visualized on post-sonication T2-W TSE images in **Figure 40D**, indicating full coverage of the tumor. The sagittal and coronal images show the formed overlapping lesion in planes parallel and perpendicular to the beam, respectively, confirming that the tumor mimic was thoroughly treated while minimizing off-target heating. The corresponding thermal profile and a T2-W TSE image of the phantom following a similar sonication through the 1-mm resin skull mimic are shown in **Figure 41**.

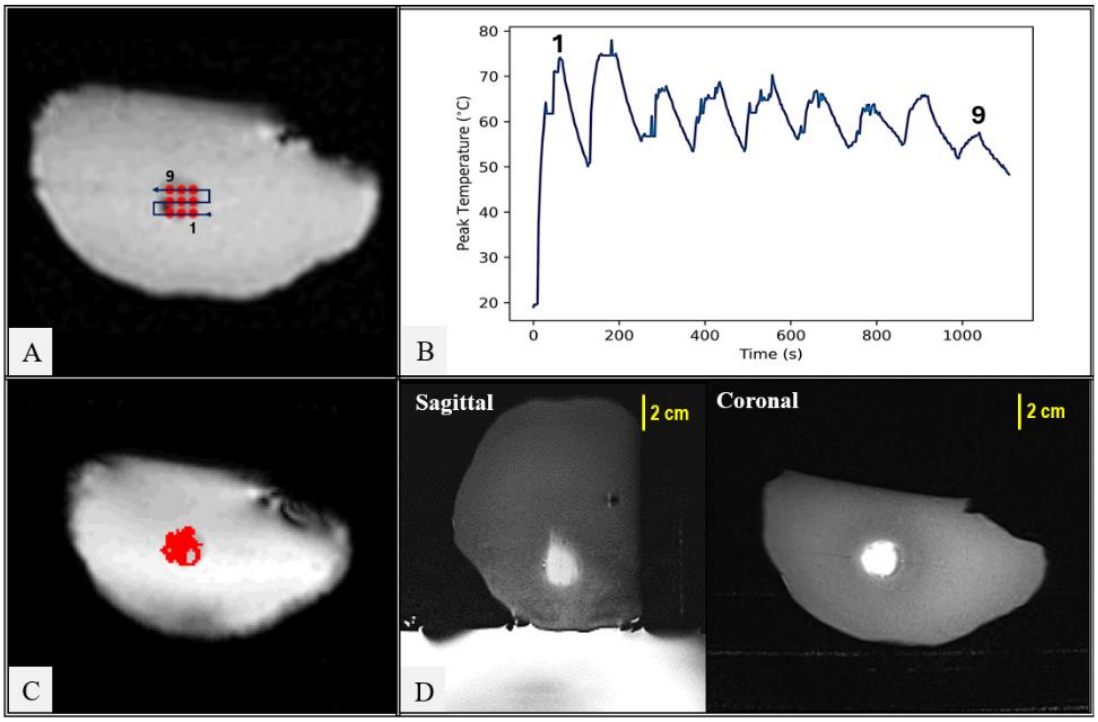

Figure 40: *(A) Planned 3x3 sonication pattern (step of 5 mm) overlaid on FLASH image of the phantom. (B) Timeseries of focal temperature evolution recorded at the nice sonication points, each exposed to 80 W (1838 W/cm^2) for 60 s with a 60-s cooling time at a FD of 35 mm, without a skull mimic. (C) Corresponding simulated necrosis map. (D) Post-sonication T2-W TSE phantom images revealing an overlapping lesion covering the entire tumor.*

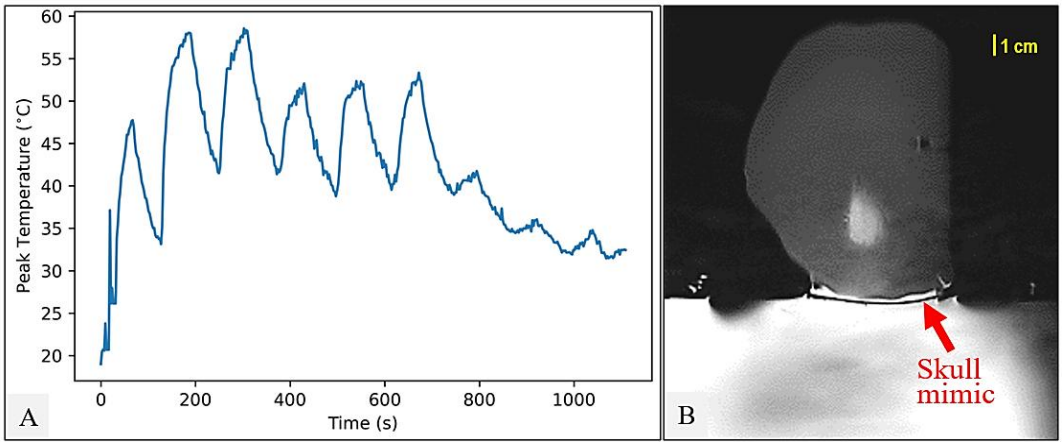

Figure 41: *(A) Timeseries of focal temperature evolution recorded at the nice sonication points, each exposed to 80 W (1838 W/cm^2) for 60 s with a 60-s cooling time at a FD of 35 mm, through the 1-mm resin skull mimic. (B) Post-sonication T2-W TSE sagittal phantom image revealing an overlapping lesion covering the entire tumor.*

3.7.2.2 Effect of Skull Thickness

Among the candidate skull mimics made from different polymers, the resin skull mimic demonstrated the best performance in terms of effectively heating deep phantom regions and accurately targeting the tumor, ensuring precise energy delivery to the intended area. As a result, additional experiments were conducted using this material to test the effect of varying skull thicknesses.

High-resolution T2-W TSE axial images acquired before the experiment (reference images), confirmed proper acoustic coupling (i.e., no presence of air) and alignment of the transducer with the skull model aperture. Relevant results are shown in **Figure 42** for both the no-skull and skull interference conditions.

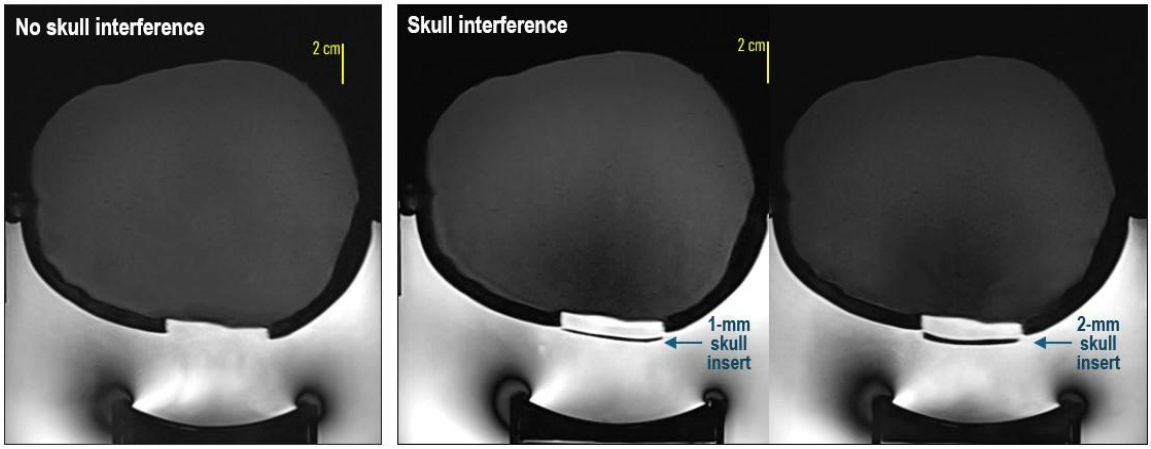

Figure 42: *T2-W TSE axial images of the head phantom positioned above the transducer, without skull insert and with the 1- and 2-mm resin skull inserts in place.*

Figure 43 summarizes the acquired MR thermometry data, with line charts presenting the temperature changes (mean values, n=10) at the focus for the five tested conditions (no skull, 1-mm skull, 2-mm skull, 3-mm skull, realistic skull) at both acoustic power levels (sonication time = 60 s, FD = 5 cm, transducer No.2). The charts demonstrate a decreasing trend in temperature change as skull insert thickness increases, with the least change observed in the case of the realistic skull. Both power levels follow a fourth-order polynomial fit. Note that, at 120 W, the temperature change decreased more rapidly with thickness.

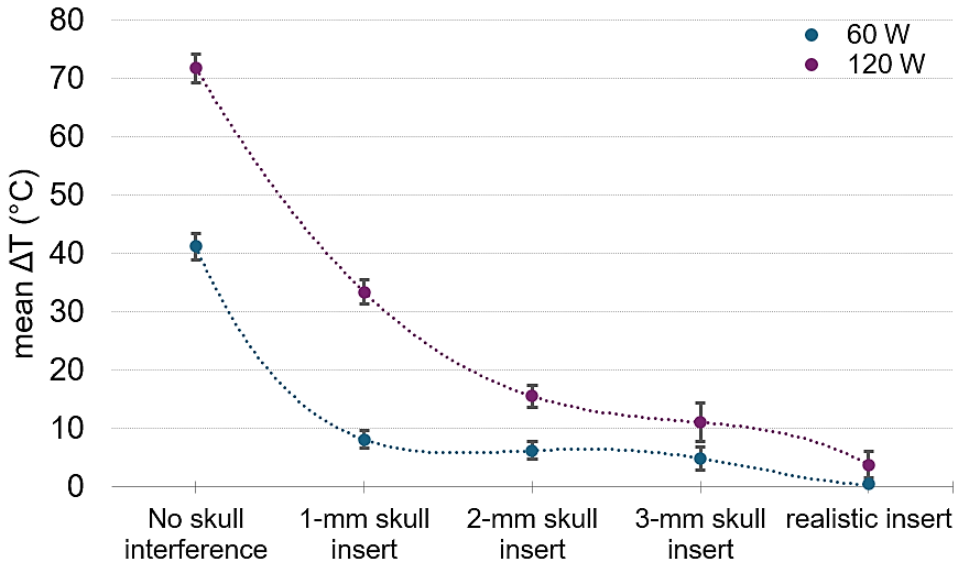

Figure 43*: Mean focal temperature change recorded at both tested power levels: without skull interference, through uniform-thickness resin inserts, and through the realistic skull insert. Error bars represent the standard deviation of the mean.*

The ANOVA test revealed significant differences in temperature changes at the focus across the five experimental conditions ($p<0.0001$). Post-hoc analysis using the Tukey HSD test demonstrated significant changes in focal temperature between the 'No Skull Interference' condition and all other conditions, as well as between the realistic insert and each uniform-thickness insert. For the higher power of 120 W, the differences among the uniformly thin inserts were statistically significant ($p<0.05$). On the contrary, in the case of 60 W, the differences between the 1-mm and 2-mm inserts, as well as between the 2-mm and 3-mm inserts, were not statistically significant ($p>0.05$).

Indicative T2-W TSE (coronal and axial) images following sonication at 120 W (6400 W/cm²) for 60 s are shown in **Figure 44**. These images specifically compare lesion formation between the no skull condition and skull interference condition for the 1- and 2-mm skull inserts. While a large hyperintense lesion was observed without skull interference, a substantially smaller lesion was detected with the 1-mm insert, and only a faint indication of a lesion was visible with the 2-mm insert. Note that for the 3-mm and realistic (varying thickness) inserts, no thermal effects were detected, and the post-sonication images resembled the reference images (**Figure 42**). In terms of thermal monitoring, **Figure 45** presents indicative temperature and thermal dose maps derived from the 60-s sonications at 60 W (3200 W/cm²).

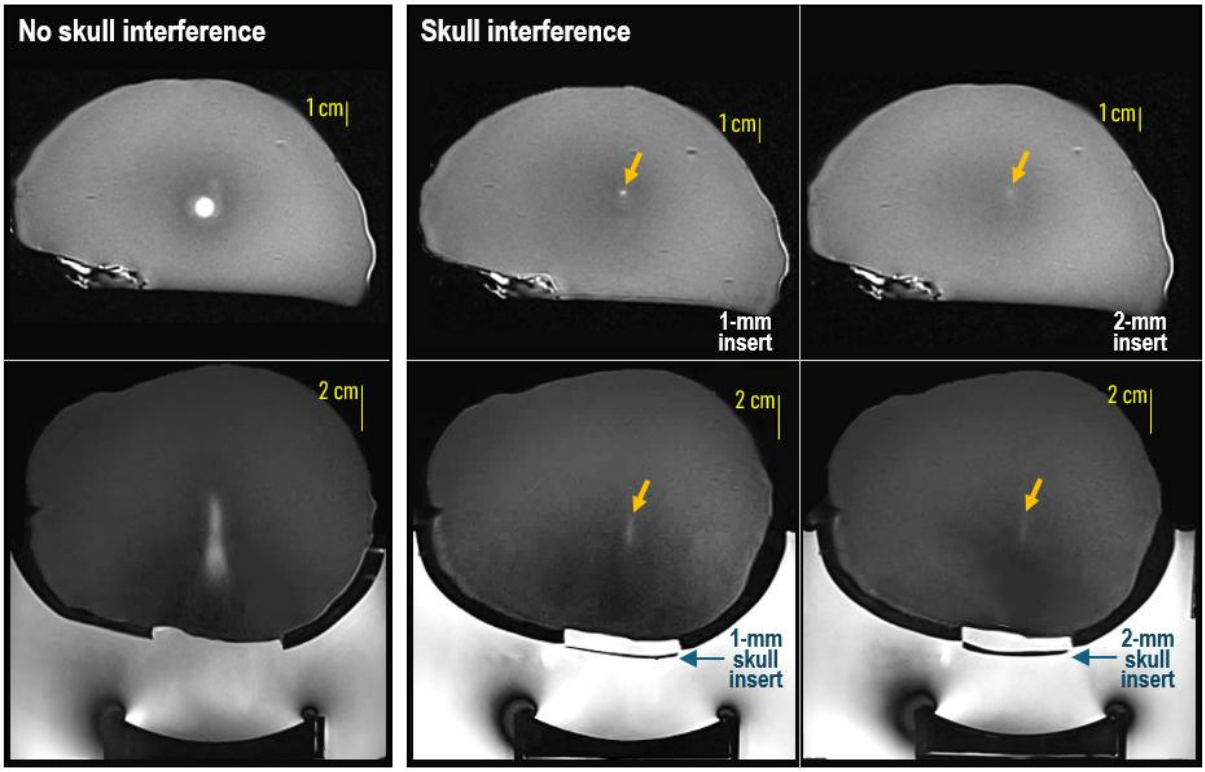

***Figure 44**: T2-W TSE coronal (top row) and axial (bottom row) images of the head phantom following 60-s sonication at 120 W (FD of 5 cm), without skull insert and with the 1- and 2-mm resin skull inserts in place.*

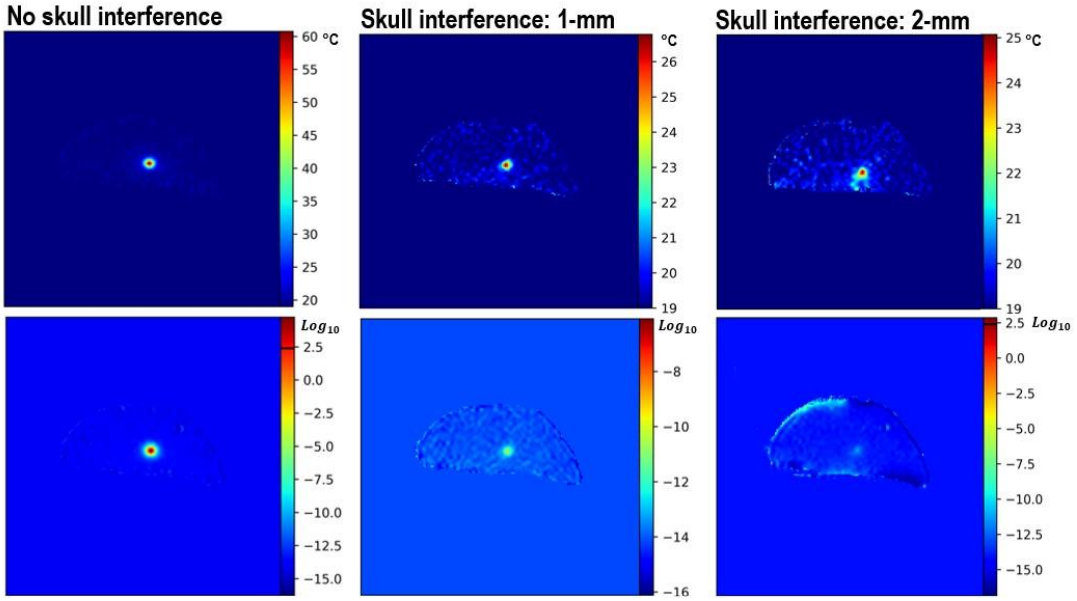

***Figure 45**: Temperature maps (top row) and thermal dose maps (bottom row) from a 60-s sonication at 60 W, without skull insert and with the 1- and 2-mm resin skull inserts in place.*

3.8 Sonication in lamb brain

Figure 46 presents representative thermometry outcomes from sonications performed in lamb brain tissue. **Figure 46A** and **Figure 46B** display coronal thermal and thermal dose maps, respectively, acquired from a sonication at an electric/acoustic power of 100/35 W for 60 s, with the FD adjusted at 20 mm. This sonication resulted in a maximum focal temperature (T_{max}) of 35 °C, corresponding to a temperature increase (ΔT) of 16 °C. **Figure 46C** illustrates the relationship between focal temperature change and increasing applied ultrasonic energy.

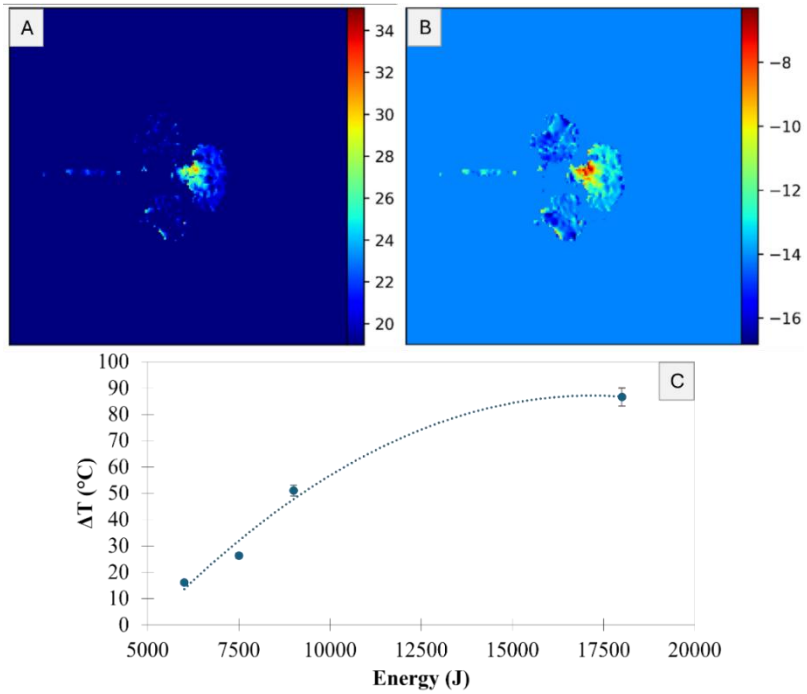

***Figure 46**: A) Coronal thermal map from sonication at an electric/acoustic power of 100/35 W for 60 s, at a FD of 20 mm. B) Corresponding thermal dose map. C) Focal temperature change versus applied ultrasonic energy.*

3.9 Preliminary Testing of Histotripsy Protocols

3.9.1 Laboratory evaluation: Effect of ultrasonic parameters on phantom erosion

Histotripsy exposures executed on the 2% w/v agar-based phantom using varied applied acoustic power successfully generated lesions at all PRPs. The mechanically fractionated liquefied regions were visible on post-sonication B-mode US images as indicatively shown in **Figure 47** (ac. power = 210 W, PRP = 750 ms). Lesions appeared as hypoechogenic areas that could be easily delineated from the surrounding undamaged echogenic phantom.

Figure 47: *B-mode US image of fractionated lesion created in a 2% w/v agar phantom after 1500 histotripsy pulses delivered at an acoustic power of 210 W and a PRP of 750 ms.*

As shown in **Figure 48a** and **Figure 48b**, the diameter and length of the histotripsy-induced lesions varied with the applied acoustic power across both PRPs, exhibiting distinct erosion patterns as the power increased. The effect of the number of applied histotripsy pulses on the diameter and length of the fractionated lesions is shown in **Figure 48c** and **Figure 48d**, respectively.

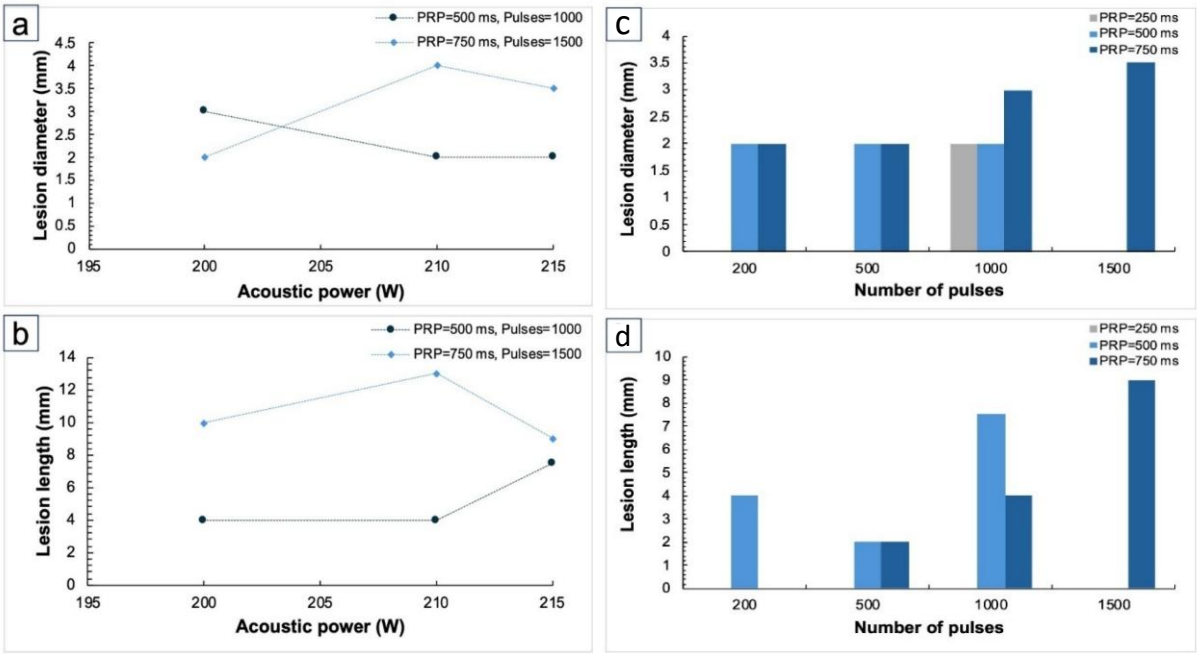

Figure 48*: Charts of lesion a) diameter and b) length versus acoustic power for a PRP of 500 and 750 ms. Bar-chart of lesion c) diameter and d) length for varied number of pulses at acoustic power of 215 W and a PRP of 250, 500, and 750 ms.*

Figure 49 presents a sagittal T2-W TSE image showing five histotripsy-induced lesions formed following identical sonications at a 750 ms PRP (1,000 bursts at an acoustic power of 215 W). The lesions appear as tadpole-shaped hyperintense areas surrounded by a hypointense rim. Measurements from the T2-W TSE image revealed an average lesion diameter of 2.31 ± 0.05 mm and a length of 15.04 ± 0.49 mm (n=5).

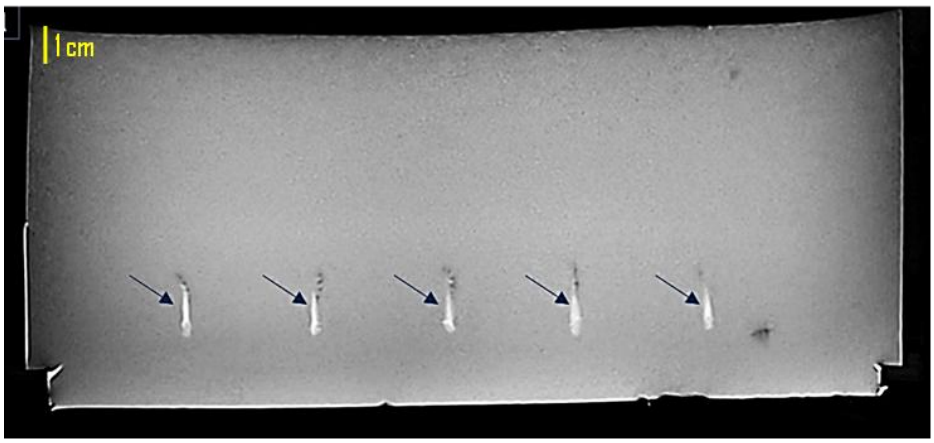

***Figure 49**: Sagittal T2-W TSE image of histotripsy lesions (blue arrows) created in a 2% w/v agar phantom after 1000-burst sonications executed at acoustic power of 215 W using a PRP of 750 ms.*

Additional results obtained from sonication at an acoustic power of 220 W, with a duty factor of 2%, PRP of 1000 ms, FD of 20 mm, PD of 20 ms, and a total of 1000 pulses are shown in **Figure 50**.

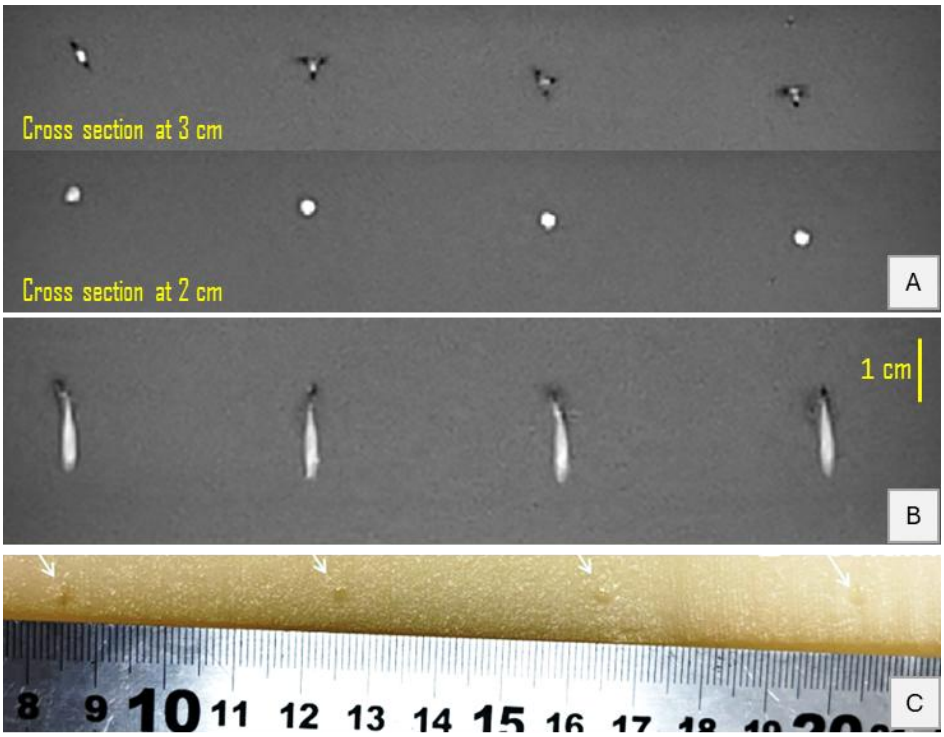

***Figure 50**: A) Coronal T2-W TSE images of the phantom at 2 and 3 cm (cross section). B) Sagittal T2-W TSE image of the phantom (parallel to the lesions). C) Photo of the actual lesions following phantom sectioning.*

3.9.2 MRI monitoring of Histotripsy lesion formation in phantom

Intraprocedural T2-W TSE imaging successfully captured histotripsy-induced phantom changes over time, as shown in the indicative outcomes in **Figure 51**. This figure displays a selection of axial T2-W TSE images from the entire series of scans, spaced at regular intervals throughout the sonication session (I_{SPPA} = 29.4 kW/cm², PRP = 1 s, DF = 2%, 2,000 pulses, FD = 2.5 cm). Progressive changes in signal intensity are visible across the imaging sequence, reflecting the dynamic response of the phantom and lesion evolution. Note that post-sonication images (>2,000 s) are also shown, clearly delineating the formed lesions, with hypointensity associated with thermal changes being resolved.

***Figure 51**: Selected axial T2-W TSE images from a series of scans, spaced at regular intervals throughout the sonication session (I_{SPPA} = 29.4 kW/cm², PRP = 1 s, DF = 2%, 2000 pulses).*

A higher-resolution T2-W TSE image acquired afterward is shown in **Figure 52**a, with corresponding coronal views at two cross-sections of the formed lesion shown in **Figure 52**b. This figure shows the characteristic appearance of histotripsy lesions on the proposed phantom in T2-W images, with hyperintense signal areas (elongated with a slightly widened tail) surrounded by a hypointense border. **Figure 52**c shows a photo of the actual lesion's cross-section at the FD, taken after phantom dissection. The mean lesion diameter from three identical sonications (I_{SPPA} = 29.4 kW/cm², PRP = 1 s, DF = 2%, 2,000 pulses, FD = 2.5 cm) was measured as 2.4 mm on MRI scans. The measurement was in close agreement with the actual lesion size of 2.3 mm, measured using a caliper. Importantly, the employed sequence effectively tracked changes in lesion dynamics in response to variations in ultrasonic parameters, further validating the phantom's ability to reflect these changes. An example of the effect of the number of pulses and RPR on lesion size is shown in **Figure 53**.

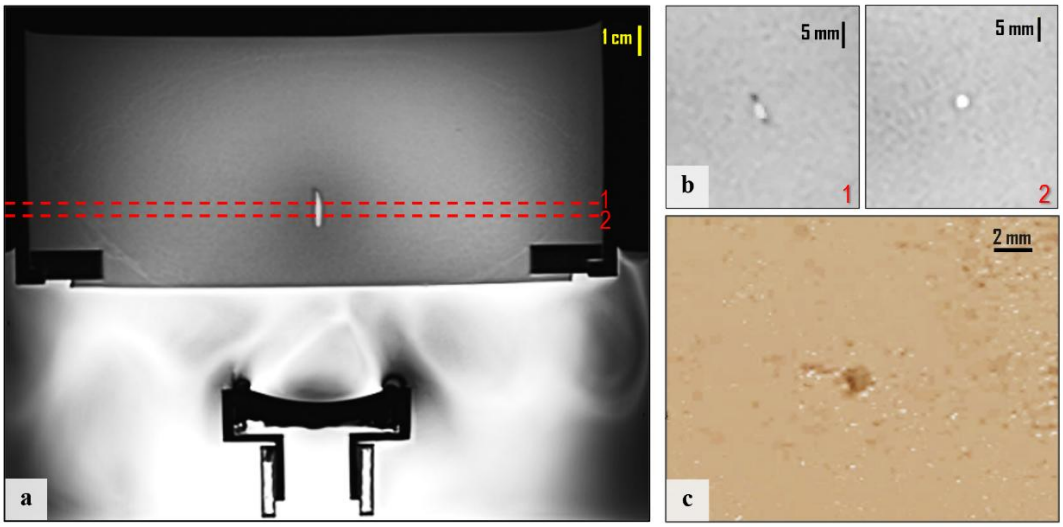

***Figure 52**: a) High-resolution T2-W TSE axial image showing the inflicted histotripsy lesion (I_{SPPA} = 29.4 kW/cm², PRP = 1 s, DF = 2%, 2,000 pulses) following resolution of thermal effects, b) Coronal slices at two different cross-sections (1 and 2) of the lesion, and c) Photo of the actual lesion after phantom cross-sectioning at FD.*

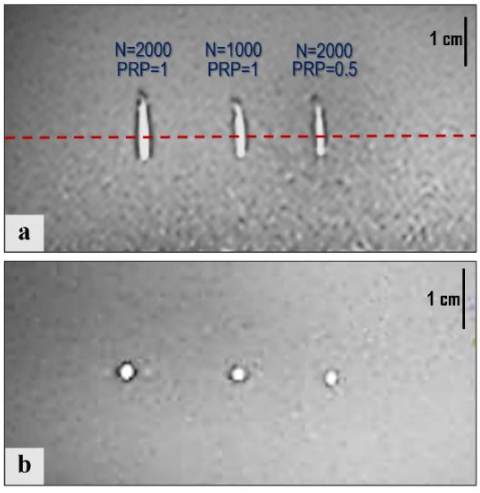

***Figure 53**: a) High-resolution T2-W TSE axial image showing histotripsy lesions created with different pulse numbers (N) and PRP (I_{SPPA} = 29.4 kW/cm² and DF = 2%), and b) Corresponding coronal slice revealing lesion diameter, with the cross-section location indicated by the red dotted line in the axial view.*

Thermal mapping data confirmed that the temperatures reached with the highest tested pulse count of 2,000 and a PRP of 1 s remained consistently below clinically relevant hyperthermia thresholds (<45°C) throughout the procedure, as shown in **Figure 54**. According to the thermal profile in **Figure 54**a, the temperature initially increased rapidly from 19°C to above 30°C within 3 minutes, then rose more gradually, almost plateauing at a maximum temperature of 34.5°C (ΔT = 15.5°C), as shown in **Figure 54**b. This corresponds to an accumulated thermal dose well below ablative levels (7.64 x 10^{-5} CEM43°C), as confirmed by **Figure 54**c.

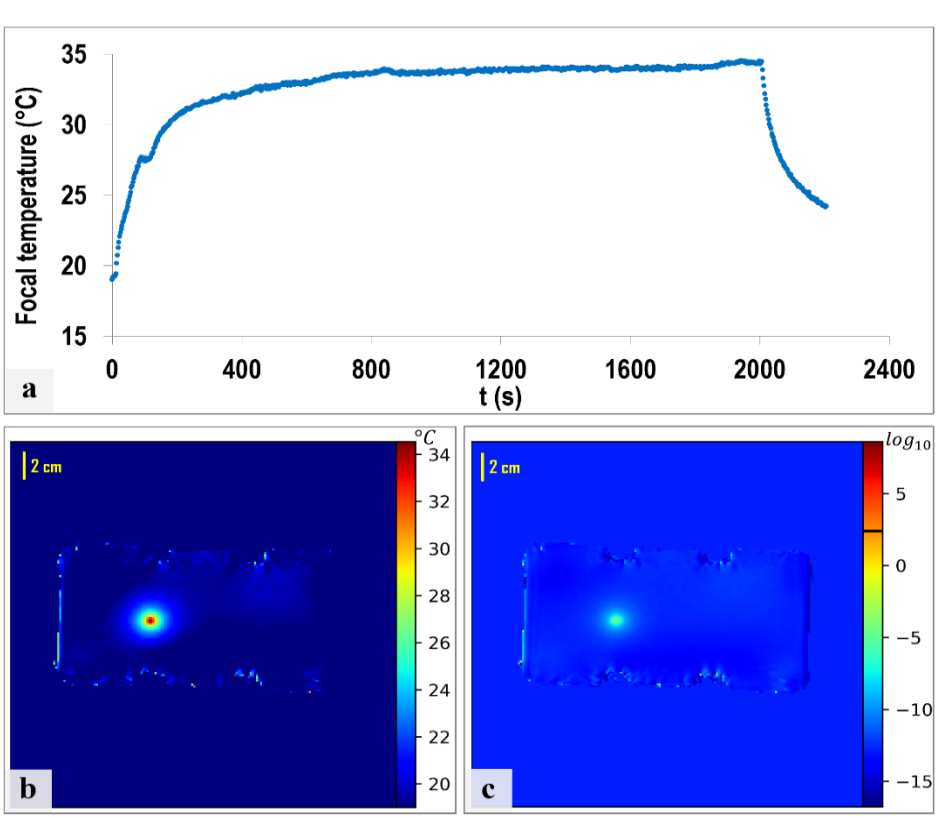

***Figure 54**: a) Focal temperature changes during and shortly after sonication (I_{SPPA} = 29.4 kW/cm², PRP = 1 s, DF = 2%, 2000 pulses), b) Colour-coded thermal map produced upon completion of sonication, and c) Corresponding thermal dose map.*

4. INTERPRETATION OF RESULTS

Both simple rectangular phantoms and anatomically realistic, tumor-bearing phantoms were employed to assess thermal heating in a 3T MRI scanner. This approach allowed for a comprehensive evaluation of the thermal performance and overall functionality of the BRAINSONIC system, including its motion accuracy, MRI compatibility, and seamless integration with the relevant software. The phantoms were prepared using agar-silica mixtures as the base material. For the plain phantom, a composition of 6% agar and 4% silica (w/v) was selected as the optimum. In the case of tumor-bearing models, the tumor region was composed of 6% agar with 4–6% silica, while the surrounding background tissue was modeled using 6% pure agar gel, providing distinct acoustic, thermal, and MRI properties between regions.

The employed optimized T2-W TSE sequence revealed FUS lesions as well-defined, hyperintense regions on the phantom. This is attributed to high-power FUS altering the MR relaxation properties of the phantom, resulting in a significant increase in T2 relaxation time within the lesion area compared to the unsonicated regions, thereby enabling clear visualization of the lesions on T2-W TSE imaging. This enhancement arises from the increase in water content induced by thermal ablation. Notably, the ability to form lesions and visualize them as hyperintense areas on T2-W images relied on the inclusion of silica.

By gradually increasing the power and monitoring the onset of lesions on T2-W images, we established the thermal dose threshold for effective lesion creation in the phantom. The threshold was defined as the level required to produce lesions with reliably measurable dimensions (in T2-W imaging), specifically those spanning at least 4 pixels in diameter. Based on this criterion, a focal temperature threshold of 39°C was established, corresponding to a thermal dose of 1.49×10^{-4} CEM43°C. The lesions exhibited rapid regression, with the time to lesion disappearance estimated at 15 minutes post-sonication. This means that the phantom can be re-sonicated after this period to ensure lesions have disappeared. Importantly, the repeatability experiment demonstrated that thermal profiling in the phantom is consistent and reliable. While some variability was observed across repetitions, the coefficient of variation was approximately 5%, which is considered sufficiently consistent for the application.

In the comparative study between the 6% agar-4% silica (w/v) phantom and excised porcine tissue, notable differences were observed in thermal behavior and lesion formation. The excised tissue exhibited variable thermal responses, likely due to inherent inhomogeneities such as compositional differences, fat content, and the presence of air; factors absent in the homogeneous phantom. Indicatively, when subjected to an 8×8 grid sonication (5 mm step, 90 W for 30 s at each point, 60-s delay), the phantom produced 64 distinct lesions precisely at the intended focal depth, accompanied by a smooth and predictable thermal profile. In contrast, the excised porcine tissue showed inconsistent temperature peaks across the sonication grid, resulting in the formation of a single, merged lesion that shifted toward the sonicated surface.

The employed experimental approach enabled the assessment of how variations in applied power, sonication duration, and FD influence FUS lesion dynamics, simultaneously providing valuable insights into the performance of the transducers and the overall robotic system and helping to optimize thermal protocols. The tested focal intensities covered a broad range typical for FUS transducers,[14] with acoustic power ranging from 75 to 120 W and sonication time

from 5 to 70 s. Increasing either the power or duration generally resulted in lesions of larger dimensions for all tested transducers. Lesion morphology; particularly the shape and extent of thermal effects, depended on the transducer's characteristics and focusing ability, resulting in variations such as elongated (cigar-shaped) lesions or lesions with increasing diameter due to near-field heating and heat diffusion. For instance, with transducer No. 3, applying at least 75 W of acoustic power for a short duration of 20 s generated tapered lesions that widened in diameter toward the transducer. This effect became more pronounced as the applied energy increased, revealing limited focusing capabilities. In contrast, the larger 1 MHz transducer (No.2) enabled sharper beam focusing deep within the phantom, reducing heat diffusion phenomena. This capability resulted in the formation of thin, cigar-shaped thermal lesions at various depths within the phantom when exposed to a high acoustic power of 120 W for up to 40 s. Therefore, the FUS system demonstrated its capability to achieve effective beam focusing and accurate lesion formation at the intended depth, without significant shifting effects, provided that an appropriately selected transducer was used.

A wall-less flow phantom model for MRgFUS preclinical research was also developed as an advanced version of the simple agar–silica gel. The multi-channel flow dynamics created in the phantom more closely mimicked conditions in the small-caliper vessel network. A constant flow rate of 38 mL/min was generated using close-fitting inlet and outlet tubes connected to a common peristaltic pump, which demonstrated reliable performance. A series of sonications were performed, centrally targeting the channel network area, with varying acoustic power levels (15-45 W) for 30-60 s. The phantom withstood repeated use and maintained structural integrity throughout these preliminary experiments, suggesting good durability. An interesting deviation in thermal response was observed in the thermal maps when compared to the static phantom. Despite employing a wall-less design to prevent attenuation from the tubing walls, the observed thermal behavior indicates a complex interaction between the FUS beam and the water-filled channels. Specifically, widespread elevated temperatures were observed below the channel network, shifted from the intended location. These observations could be attributed to two complementary mechanisms. First, as the FUS wave propagates through the multi-channel network, it encounters the lower channels first, where initial heating and dissipation occur. This likely establishes a temperature gradient, causing heat to be preferentially transferred downward. Simultaneously, multiple small reflections at the phantom-water interfaces may contribute to localized energy redistribution, intensifying heating in unintended regions. Follow-up studies will help clarify these assumptions.

We further introduced an anatomically precise head phantom containing a tumor mimic, enabling a more rigorous investigation of various MRgFUS protocols for both partial and robotic-assisted complete tumor ablation. As a representative example, applying 1600 J of ultrasonic energy to the tumor mimic with transducer No. 3 produced a cigar-shaped lesion, which evolved into a more pronounced egg-shaped form at 2400 J. Overlapping lesions were successfully created to cover a 2-cm tumor located at a depth of 3.5 cm within the phantom, using robotic-assisted grid sonication with a representative 3×3 pattern. Each focal point received 80 W (1838 W/cm^2) for 60 s, followed by a 60-s cooling interval.

The effect of 1-mm skull mimics, 3D-printed with three different polymers (Resin, ASA, and TPU), on FUS energy transmission and deposition in the tumor was investigated. Thermal

effects were compared to the unobstructed-field scenario, where no skull was present. In the no-skull condition, the highest energy deposition occurred within the tumor mimic, as anticipated. A typical focal intensity of 1838 W/cm² applied for 30 s resulted in a temperature increase of 65.1°C at the focal spot. In the presence of the resin skull, a notable reduction in energy deposition was recorded, yet the temperature increase remained relatively high at 50.7°C, which is approximately 20% lower than the unobstructed-field condition. In contrast, ASA and TPU plastics led to a limited temperature increase of less than 10 °C; representing a reduction of over 90% compared to unobstructed sonication, indicating substantial obstruction of energy transmission. Thicker resin inserts of 2 mm and 3 mm were also tested; however, they resulted in reductions of more than 60% in focal temperature compared to the no-skull condition. Therefore, the potential of brain tissue ablation through thicker skull inserts was deemed infeasible.

Further sonication experiments were carried out using the 1-mm resin skull due to its superior acoustic performance, which enabled the formation of well-defined lesions within the tumor mimic. Building on these findings, grid sonication through the 1-mm resin skull insert was evaluated and yielded consistent results, further supporting its effectiveness for transcranial lesion targeting. In a representative 3×3 grid sonication pattern (1838 W/cm² for 60 s at each point, with a 60 s delay), the mean temperature across the nine focal points in the presence of the resin skull was 48.4 ± 8.2 °C, compared to 68.1 ± 5.5 °C without skull interference. The increased standard deviation indicates greater variability in temperature outcomes, suggesting that the skull mimic may cause inconsistencies in energy deposition during grid sonication. Despite this, complete coverage of the tumor mimic was achieved, demonstrating accurate heating with no observable off-target effects.

The reasoning for exploring the implementation of a 1-mm skull mimic lies in the idea that temporarily excising a small section of the human skull and replacing it with a thin, biocompatible insert could enable FUS ablation of inoperable brain tumors using a simple single-element ultrasonic source. This approach would facilitate ablation by minimizing the intense beam aberration caused by variations in skull thickness, while leveraging the advantages of single-element transducers, such as their simplicity and cost-effectiveness compared to phased array transducers.

Preliminary histotripsy trials were conducted to explore and extend the potential applications of the BRAINSONIC system. A pure 2% w/v agar gel was used as a cost-effective and easily manufactured model, confirmed to be responsive to histotripsy. The histotripsy protocol was refined through systematic benchtop testing of how acoustic power and PRP influence phantom erosion. The selected protocol successfully produced a liquefied core within the phantom, which appeared hyperintense on T2-W images. A thin hypointense border was observed around phantom lesions, remaining stable over time—suggesting it was not due to transient thermal effects but rather a localized increase in gel density, likely caused by mechanical compaction. T2-W TSE imaging, using parameters optimized to balance temporal resolution and image quality, effectively captured histotripsy-induced signal changes, revealing the progressive development of lesions, with imaging updates every 10 s.

5. CONCLUSIONS

The proposed agar/silica tissue-mimicking phantoms offer a controlled environment for preclinical MRgFUS assessments. Their predictable response to variations in power and duration, along with their homogeneity, enables the formation of symmetric, cigar-shaped lesions in defined patterns, making them ideal for evaluating the heating performance and long-term reliability of MRgFUS systems, and supporting their use in calibration and quality assurance. Compared to excised animal tissue, they provide significant advantages, including enhanced reproducibility, reusability, ease of handling, cost-effectiveness, and the elimination of ethical concerns. Through a series of single-point and grid sonications, the heating capabilities of the BRIANSONIC system were successfully demonstrated. These tests confirmed reliable performance without malfunctions, accurate motion control, and seamless communication with the software. Furthermore, the software functionalities for treatment planning and intra-procedural monitoring operated as intended. The system also proved to be user-friendly, supporting an efficient and intuitive workflow within the MRI environment. Importantly, the promising results of precise thermal ablation of tumor mimics through the 1-mm resin skull model provided proof of concept for the proposed innovative therapeutic approach, i.e., treating inoperable brain tumors using FUS thermal ablation delivered through dedicated skull implants. If proven feasible, this approach could address key challenges in FUS brain tissue ablation by avoiding the intense beam aberration caused by the human skull and enabling efficient ultrasonic energy delivery to any brain region, all while requiring only a minor craniotomy. Therefore, BRAINSONIC has the potential to provide a minimally invasive method for ablating brain tumors using a thin, biocompatible implant, allowing for repeated treatments and offering therapeutic options for both inoperable and recurrent cases.

REFERENCES

1. Antoniou A, Georgiou L, Evripidou N, Ioannides C, Damianou C. Challenges regarding MR compatibility of an MRgFUS robotic system. Journal of Magnetic Resonance 2022;344:107317.
2. Rieke V, Butts Pauly K. MR thermometry. Journal of Magnetic Resonance Imaging 2008;27(2):376–90.
3. Bing C, Staruch RM, Tillander M, Köhler MO, Mougenot C, Ylihautala M, et al. Drift correction for accurate PRF-shift MR thermometry during mild hyperthermia treatments with MR-HIFU. Int J Hyperthermia 2016;32(6):673–87.
4. Sapareto SA, Dewey WC. Thermal dose determination in cancer therapy. Int J Radiat Oncol Biol Phys 1984;10(6):787–800.
5. ter Haar G, Coussios C. High intensity focused ultrasound: Physical principles and devices. International Journal of Hyperthermia 2007;23(2):89–104.
6. Jolesz FA. MRI-Guided Focused Ultrasound Surgery. Annu Rev Med 2009;60(1):417–30.
7. Antoniou A, Evripidou N, Georgiou L, Chrysanthou A, Ioannides C, Damianou C. Tumor phantom model for MRI-guided focused ultrasound ablation studies. Med Phys 2023;50(10):5956–68.
8. Korthuis RJ. Regulation of Vascular Tone in Skeletal Muscle. In: Granfer N, Granger J, editors. Skeletal Muscle Circulation. Morgan & Claypool Life Sciences; 2011.
9. Sotornik R, Brassard P, Martin E, Yale P, Carpentier AC, Ardilouze JL. Update on adipose tissue blood flow regulation. American Journal of Physiology-Endocrinology and Metabolism 2012;302(10):E1157–70.
10. Drakos T, Giannakou M, Menikou G, Constantinides G, Damianou C. Characterization of a soft tissue-mimicking agar/wood powder material for MRgFUS applications. Ultrasonics 2021;113:106357.
11. Zeng T, Chen H, Yoshitomi T, Kawazoe N, Yang Y, Chen G. Effect of Hydrogel Stiffness on Chemoresistance of Breast Cancer Cells in 3D Culture. Gels 2024;10(3):202.
12. Antoniou A, Evripidou N, Giannakou M, Constantinides G, Damianou C. Acoustical properties of 3D printed thermoplastics. J Acoust Soc Am 2021;149(4):2854–64.
13. Antoniou A, Damianou C. Feasibility of Ultrasonic Heating through Skull Phantom Using Single-element Transducer. J Med Ultrasound 2024;32(1):32–40.
14. Zhou YF. High intensity focused ultrasound in clinical tumor ablation. World J Clin Oncol 2011;2(1):8–27.